University of Neuchâtel
Physics Departement

Cryogenic Detectors as High-Efficiency Detectors of Single Massive Macromolecules

Thesis by
Daniel R. Gerber

in Partial Fullfillment of the Requirements
for the Degree of
Docteur ès Sciences

In presence of a jury composed by
Prof. Dr. J.-L. Vuilleumier, thesis advisor, Neuchâtel
Prof. Dr. P. Martinoli, Neuchâtel
PD Dr. D. Twerenbold, Neuchâtel
Prof. Dr. E. Schumacher, Berne

Fall 1997

IMPRIMATUR POUR LA THÈSE

Capteurs cryogéniques comme détecteurs à haute efficacité pour les macromolécules lourdes

de M. Daniel Gerber

UNIVERSITÉ DE NEUCHÂTEL
FACULTÉ DES SCIENCES

La Faculté des sciences de l'Université de Neuchâtel sur le rapport des membres du jury,

MM. J.-L. Vuilleumier (directeur de thèse),P. Martinoli, D. Twerenbold et E. Schumacher (Université de Berne)

autorise l'impression de la présente thèse.

Neuchâtel, le 5 juillet 1998

Le doyen:

F. Stoeckli

to my Gogy

Contents

Abbreviations and Units

Special units

Dalton (Da) is a commonly used mass unit in the field of mass spectrometry. 1 Da is equal to the one-sixteenth the mass of the atom oxygen of mass number 16. One Dalton corresponds approximatively to the mass of one proton.

Kelvin (K) is the temperature scale were the absolute zero is taken as the starting point. 0 K $\hat{=}$ -273.15 °C

Electronvolt (eV) is an energy unit: 1 eV is equal to the energy gained by an electron in passing a potential difference of one volt; 1keV = 1000 eV.

Useful constants

k_B	=	$8.617 \cdot 10^{-5}\,\mathrm{eV} \cdot \mathrm{K}^{-1}$	Boltzmann's constant
	=	$1.38 \cdot 10^{-23}\,\mathrm{J} \cdot \mathrm{K}^{-1}$	
$\hbar$	=	$6.5822 \cdot 10^{-16}\,\mathrm{eV} \cdot \mathrm{s}$	Planck's constant
m_p	=	$1.6726 \cdot 10^{-27}\,\mathrm{kg}$	Proton rest mass
N_A	=	$6.022 \cdot 10^{23}\,\mathrm{mol}^{-1}$	Avogadro's constant
e	=	$1.60219 \cdot 10^{-19}$ Coulomb	Electron charge
c	=	$2.997925 \cdot 10^{8}\,\mathrm{m} \cdot \mathrm{s}^{-1}$	Speed of light

$$
\begin{aligned}
1\ \mathrm{eV} &\leftrightarrow 2.41796 \cdot 10^{14}\,\mathrm{Hz} \\
&\leftrightarrow 8.0655 \cdot 10^{3}\,\mathrm{cm}^{-1} \\
&\leftrightarrow 1.1604 \cdot 10^{4}\,\mathrm{K}
\end{aligned}
$$

Abbreviations

NIST	:	National Institute of Standards and Technology; Boulder, Colorado, USA.
GMU	:	George Mason University; Fairfax, Virginia, USA.
PSI	:	Paul Scherrer Institut; Villigen, Switzerland.
MS	:	Mass spectrometry, mass spectrometer
TOF	:	Time-of-Flight
MALDI	:	Matrix Assisted Laser Desorption/Ionization
ESI	:	Electrospray ionization
UV	:	Ultraviolet; electromagnetic waves with a wavelength between 3 nm and 400 nm.
MCP	:	Microchannel Plate
SEM	:	Secondary Electron Multiplier
FWHM	:	Full-width at half maximum
STJ	:	Superconducting Tunnel Junction
SIS	:	Superconductor-Insulator-Superconductor
NIS	:	Normal-Insulator-Superconductor
qp	:	quasiparticle
Sn	:	Tin
Nb	:	Niobium
Ag	:	Silver
Si	:	Silicon
Al	:	Aluminium
BSA	:	Bovine Serum Albumin, 66 kDa
IgG	:	Immunoglobulin G, 130 kDa
3-HPA	:	3-Hydroxypicolinic acid (matrix)

Introduction

Mass spectrometry is a fast, accurate and sensitive analytical tool for obtaining molecular weight information. Until 1987, the measurable mass range was limited by thermal instability of heavy biological molecules. New ion production techniques had to be developed in order to vaporize and ionize efficiently massive macromolecules without fragmentation. In Section 1.1 of this thesis, we retrace the historic way leading to the two well-established ion sources meeting this requirements: the Matrix-Assisted Laser Desorption/Ionization (MALDI) and the Electrospray Ionization (ESI).

Once the ion production problem solved, one realized (see Section 1.3) that the limiting factor was now the low detection efficiency of the state-of-the-art ion detectors based on the secondary electron emission (e.g. microchannel plate MCP).

As a way-out of this impasse, Twerenbold proposed [1] in 1995 the use of cryogenic particle detectors previously developed for applications such as X-ray spectroscopy and searches for nonbarionic dark matter. As shown in Chapter 2, these detectors are based on a radically different detection scheme: Upon impact, the (kinetic) energy of the particle is absorbed and transformed into a measured increase of the internal energy of the detector. In order to run these detectors properly, low temperatures – often below one Kelvin – are required.

Owing to this calorimetrical detection scheme one can expect an impact detection efficiency for single macromolecules of 100%, independent of the mass. Furthermore, since the pulse height is proportional to the kinetic energy which itself depends linearly on the charge of the molecular ion, one can expect that it would even be possible to determine the charge state as well – a feature not covered by any conventional detector.

Knowing the charge q will be very helpful to deconvolute mass spectra since mass analyzers give a measure of the mass-to-charge ratio m/q and not the mass m alone (see Section 1.2).

As Ph.D. thesis task I had the chance to take part on three experiments which have been performed to prove the above mentioned assumptions.

Up to now, all the experiments which detected macromolecules with cryogenic detectors were performed with Matrix-Assisted Laser Desorption/Ionization time-of-flight mass spectrometers (MALDI-TOF MS). Section 1.4 of this text defends this choice.

The first experiment ever done in this field has been undertaken by the Neuchâtel/GMU/PSI collaboration at the Physics Institute of Neuchâtel.

As we intended in a first time just to observe if it is in principle possible to detect impacts of macromolecules with a cryogenic particle detector, a straightforward, home-built mass spectrometer was used. Some easily made shadow-mask SIS tin junctions were used as cryogenic detectors (see Section 3.3.1).

From obtained results, presented in Chapter 4 and in [2], we can affirm that we were detecting single macromolecule impacts of the protein lysozyme (molecular weight = 14'300 Da[1]). A calibration with 6 keV X-rays suggested that a substantial part of the kinetic energy (10 keV) was absorbed in the detector.

Additionally, an indication was found that the pulse height does, as predicted, depend on the charge state of the detected molecule. To further investigate this point, detectors with a better energy resolution had to be developed. This is why we decided to fabricate tin junctions using photolithographic techniques; the obtained devices are presented in Section 3.3.3.

Meanwhile, we participated in the NIST/Neuchâtel/GMU collaboration. The measurements were performed at the National Institute of Standards and Technology in Boulder CO, USA. They provided the detector, a hot-electron microcalorimeter (see Section 3.3.2), mounted on their adiabatic demagnetisation refrigerator (ADR) while we provided a small home-fabricated MALDI-TOF mass spectrometer.

Although the working principle of this microcalorimeter is significantly different, comparable results have been obtained, as reported in Chapter 5 and in [3]. This underlines that the high-efficient detection of macromolecules is a generic attribute of cryogenic detectors.

With this microcalorimeter, single impacts of the proteins immunoglobulin G (IgG; 130 kDa), lysozyme and bovine serum albumin (BSA; 66kDa)

[1]Mass unit. 1 Da = $1/16^{th}$ of the mass of a oxygen atom; essentially the mass of a proton.

have been detected. Due to the energy resolving capability of this detector, the charge state of the molecular ions could be clearly determined.

It was found that the proteins deposit roughly 50% of their kinetic energy in this microcalorimeter and that the good energy resolution for 6 keV X-rays is considerably degraded for ion impacts. Finally, this experiment illustrated the need for a good vacuum in the mass spectrometer.

After having succeeded in fabricating tin SIS junctions using photolithographic techniques (Section 3.3.3) we resumed the mass spectrometric work in Neuchâtel with an upgraded equipment. Notably an ion optic and two delayed extraction units have been incorporated. The energy resolution of these better tin tunnel junctions was sufficient to discriminate between singly and doubly charged ions. In Chapter 6 we present some results obtained with the proteins IgG and lysozyme showing time-of-flight spectra, the charge separation capability of our detectors and the interesting fact that we observe the same pulse height for 6 keV X-rays and ions with the same energy.

And finally, we achieved getting time-of-flight spectra of DNA-oligonucleotides with a length of up to 120 bases. The comparable peak heights of the 40-mer, 70-mer and 120-mer indicate that the launch, ionization and detection efficiencies are the same for the used oligonucleotides.

Chapter 1

Mass spectrometry

Mass spectrometry (MS) is a branch of science that determines masses by analysing the mass-dependent movement of *charged molecules* traversing electric and/or magnetic fields. In the past many techniques have been developed to extend the analyzable mass range to the field of macromolecules with masses above 100 kDa [7].

Since the MS is restricted to the *gas-phase ionized molecules*, we will review the methods of vaporization and ionization of samples in the first section of this chapter. The second section deals with the mass analyzers and the third one with the ion detectors. The last one defends our choice of working with a MALDI-TOF mass spectrometer.

1.1 Vaporization and ionization of the sample

Until the early seventies, the mass spectrometry was governed by thermal evaporation and subsequent ionization by electron impact (EI)[8]) or chemical ionization (CI)[9]) of the analyte. Electron impact ionization is a widely used technique in MS: the neutral gas-phase analyte is ionized by impact of an electron usually emitted by a tungsten filament. In the case of chemical ionization, the volatilized molecules react with a reagent gas to form ions by either proton or hydride transfer.

The molecular weight range of both techniques is limited to about 800 Da. This is caused by the fact that large molecules are thermolabile and their vapour pressure is low because of their weight and often polar nature; they thermally decompose a long time before an acceptable vapour pressure is reached.

Consequently, several new techniques had to he developed at the time in order to enahle measuring the mass of large hioorganic molecules. Two distinct ways of filling up this require appeared [10]: the liquid-phase ion sources and the solid-state ion sources.

In the first case, an analyte containing solution is *continuously sprayed* into the entry stage of the ion source, where a drying gas is at atmospheric pressure. There, the droplets are drying in order that the hare analyte ions can he transferred via some differential pumping stages into the high-vacuum part of the mass spectrometer, where the mass analyzer and ion detector are located. The ionization mechanism is a *near-equilibrium, reversible* process.

For the solid-state ion sources a *non-equilibrium, non-reversible* process is needed for the volatilization of the solid sample. Based on the work of Beuhler et al. [11], a 'rapid heating' hy a 'sudden energy' release of an energetic particle or a laser pulse will desorh the sample molecules so fast that they do not have the time to thermally disintegrate.

1.1.1 Liquid-phase ion sources

Nowadays there are three liquid-phase ion sources, slightly different each one. They are based on the electrospray ionization (ESI)[12, 13, 14], the atmospheric pressure ion evaporation (APIE)[15] and on thermospray (TS)[16]. They have in common – as already mentioned – that the solution containing the analyte is sprayed steadily into the drying-gas (nitrogen).

Since we have not heen using any liquid-phase ion source hy now, but planed to do so in a near future with ESI, we will only present schematically the ion-production process in a ESI module.

The electrosprayed droplets are charged by an electric field (see Figure 1.1); the initial droplet diameters are 1-2μm [15]. They undergo a drying- and size-reduction scenario which was first described by M. Dole who pioneered the electrospray ionization in 1968: As these droplets are evaporating the solvent, the surface charge density is increasing until the electrostatic repulsion is equal to the surface tension (Rayleigh limit). The droplet is not stahle anymore and undergoes the "Coulomh explosion" producing a few smaller droplets which will themselves explode until the analyte ion itself is electrostatically ejected [18]. The charge state of the ion reflects the number of charges it carried in the solution phase. For large macromolecules highly charged states can be obtained (few hundreds). This is heneficial if one wants

to investigate massive molecules using a mass spectrometer which is limited in m/q sensitivity. So it was possible to measure electrosprayed 200 kDa molecules using a quadrupole mass spectrometer limited in m/q to 2400 [17].

The bare ion is then moved to the mass analyzer through a differential pumping stage (nozzle and skimmer).

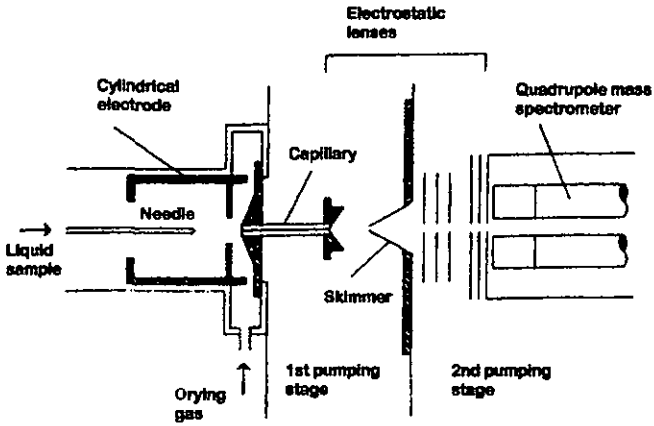

Figure 1.1: Illustration of an electrospray ion source coupled to a quadrupole mass spectrometer. The sample solution is introduced at a low flow rate (a few μl/min) through a needle held at high potential (few kV) with respect to the cylindrical electrode. Its polarity selects if positive or negative ions are transferred to the high-vacuum part. Two pumping stages are used in this case. (Figure reproduced from [12]).

An ESI spectrum can be difficult to understand – especially in the case of a mixture of analyte – since each analyte gives rise to many peaks due to multiple charging. However, an ESI ion source can be directly coupled to a chromatograph, which turns out to decrease the complexity of the mass spectra in many cases.

1.1.2 Solid-state ion sources

The first solid-state ion source was the field-desorption (**FD**), introduced by Beckey [19]. The diluted analyte is dipped on a metallic point and after the evaporation of the solvent, a strong electric field ($> 10^9$ V/cm) will bring the ionized sample to the gas-phase. But FD was too cumbersome to make a dent in the real-world mass spectrometric research.

In 1974 Torgesson and Macfarlane invented the plasma-desorption (**PD**) [20]), where the sample is vaporized by high energy ions ($\approx$100 MeV) produced through spontaneous fission of ^{252}Cf. The radioactive decay of ^{252}Cf produces two fission fragments flying apart in opposite direction. One fragment hits the sample surface knocking out a few sample ions typically, the other one is detected in a scintillator triggering the data acquisition when measuring the time-of-flight. Biopolymers up to 45 kDa [21] could be successfully volatilized with this method. Since the fission rate of a typical ^{252}Cf source is limited to a few thousand Bq, the ion current is very small, so only time-of-flight (TOF) mass spectrometers couple efficiently with PD. Anyway, the Fourier-transform mass spectrometers have also been used.

A similar approach developed approximately at the same time in Benninghovens' group [22] was the secondary ionization mass spectrometry (**SIMS**) which consists of bombarding a surface containing the sample in solid form with an 10 keV ion beam (usually ^{3}He$^+$, ^{16}O$^+$ or ^{40}Ar$^+$). This primary ions sputter off material into the gas phase: about 1% of the ejected matter is ionized. In the beginning they worked with high beam currents which caused erosion and heating up of the sample layer destroying any thermally labile molecule. An ion source working with high primary ion currents is called *dynamic* as a contrary to *static* ones working with very weak currents which do not ravage the surface quickly. Static ion sources yield spectra similar to those from PD but suffer from rather weak analyte ion currents so that they can not be coupled to scanning instruments like quadrupole and magnetic sector mass spectrometers.

The fast-atom bombardment (**FAB**[1]) invented by Barber et al. [23] circumvented the disadvantage of the dynamic secondary ion source by using a very viscous nonvolatile fluid doped with the analyte as the target instead of a solid one. Now very high primary ion/atom currents can be used because the destroyed surface is constantly removed by convection and diffusion. The beam consists of typically Ar or Xe, in form of atoms or ions. Owing to its high analyte ion current, a FAB ion source can be coupled to scanning mass spectrometers like sector instruments giving a good mass resolution. The mass range is limited to $\approx$10 kDa due to fragmentation.

[1]Sometimes the name FAB is restricted to the case where atoms are the projectiles and is called liquid-SIMS (LSIMS) or fast ion bombardment (FIB) when an ion beam is used.

An other technique is the laser ionization (LIMS) which is quite similar to SIMS: an energetic laser pulse with a certain wavelength (that will be resonantly absorbed by the sample) hits the surface where the analyte dwells in solid form. The created microplasma desorbs and ionizes some molecules of masses up to 1 kDa with minimal fragmentation but dissociation becomes domioant above this mass [24]. Thus LIMS was coosidered inferior to SIMS. LIMS is usually coupled to a time-of-flight mass spectrometer due to the intrinsic pulsed desorption.

In the late eighties two different way-outs for LIMS, both introducing the concept of **matrix**, were proposed. The main change is that the analyte is embedded in a matrix which absorbs now the laser beam energy.

The matrix used by **Tanaka** et al. [25] was a mixture of glycerol with ultra-fine cobalt powder (ø 300 Å), small enough to couple to the laser light. It can desorb molecules with masses up to 100 kDa breaking the mass record previously held by PD, but the Matrix-Assisted Laser Desorption/Ionization (**MALDI**) process had surpassed everything else.

1.1.3 MALDI (Matrix-Assisted Laser Desorption/Ionization)

Karas and Hillenkamp's group announced in 1987 the MALDI scheme [26, 27] that provides the desorption and ionization of heavy molecules (> 500 kDa) with a low fragmentation rate and a low charge state (typically 1 to 2). The technique consists of diluting the analyte in a matrix with a molar ratio of 1:500 to 1:10'000. A few μl of this analyte-matrix mixture is dropped on an inert sample holder and let to be co-crystallized. A short laser pulse of a few ns with an appropriate wavelength will desorb the sample ions.

There are two main reasons to use a matrix:

- The small matrix molecules are absorbing **resonantly** the laser beam energy. The energy transfer to the moderately absorbing analyte molecules is slow avoiding excessive energy that can cause the thermal decomposition.
- The matrix acts as a separator. It isolates one analyte molecule from the other preventing aggregation.

The wavelength of the laser must be either in the far UV to couple to the electronic states of the matrix molecules or in the far IR which can excite vibrational states. Several matrices were found to be suitable: initially nico-

tinic acid[2] [26] has been used, later on sinapinic acid[3] has proven to be superior [28]. Anyway, there is no unique matrix – each type of sample needs its own matrix. In Chapter 3 we describe the way we are producing our MALDI-probes.

MALDI is a threshold phenomenon [29]: a minimal laser irradiance[4] – the so-called 'threshold irradiance' – is needed to ignite the desorption. A laser pulse surpassing this threshold causes a rapid phase change of the MALDI-probe in the spot zone giving raise to an ion yield steeply increasing with the irradiance. This tells us that we are facing a collective process rather than a 'molecular evaporation'. Referring to [10] it would thus be more precise to talk about 'ablation' than 'desorption'. It has been shown [30, 31] that for common laser pulse lengths it is rather the laser fluence[4] which is decisive than the irradiance; about $20\,\mathrm{mJ/cm^2}$ are required.

With increasing fluence the fragmentation probability as well as the mass peak width are increasing [31] indicating that one should work close to the threshold. Beavis and Chait found, that the regulation of the laser irradiance is the most important operational parameter to obtain high mass resolution spectra [32].

To get an idea, the number of produced molecular ions per laser desorption event is of the order of 10^4; the number of ejected neutrals exceeds the number of ions by a factor of 10^3 – 10^4 ([29], measured with bovine insulin: 5.5 kDa). Bahr et al. measured even $\approx 10^6$ ions of each species per laser desorption event [45].

It has been found that the ablated analyte ions do all have approximately the same velocity regardless their mass[6]. The average velocity is between 500 m/s and 1000 m/s depending on the experiment [33, 31, 10]. The matrix ions are somewhat faster. Both velocity distributions are mainly forward peaked. However, the fact that there is a initial velocity *distribution* is of great importance in the case of TOF measurements since they limit the achievable mass resolution. In Section 1.2.3 two techniques used to iron out this problems are presented.

Thanks to MALDI, extremely large biomolecules can be vaporized and

[2] 123 Da; usable wavelengths: 266 nm, 2.94 μm and 10.6 μm [27]

[3] 224 Da; 266 nm, 337 nm, 355 nm, 2.79 μm, 2.94 μm and 10.6 μm [27]

[4] Fluence is defined as the laser beam energy per unit area at the target surface and the irradiance is the fluence per unit time.

[6] We are talking here about zero acceleration field.

ionized[7]. MALDI spectra are simple since mainly singly charged ions are produced with little or no fragmentation. MALDI is – unlike other ionization methods for macromolecules (including ESI) – generally insensitive to contaminants and is a high sensitive process: often 1 pmol of the analyte is sufficient for an analysis. More about MALDI can be found in [10, 31, 35].

1.2 Mass analyzers

The mass analyzer is the part of the mass spectrometer which spreads the ion trajectories depending on their masses. An ion of charge q and mass m, residing in an electro-magnetic field ($\vec{E}$,$\vec{B}$), is influenced by the force:

$$\vec{F} = m \cdot \ddot{\vec{x}} = q \cdot \left(\vec{E} + \dot{\vec{x}} \wedge \vec{B} \right) .$$

Let us recall that static magnetic fields do not change the energy of the ion. Almost always an electric field is used to accelerate the ions away from the ion source toward the mass analyzer. If an ion is flying across a perpendicular $\vec{B}$ ($\vec{E}$)-field, then the radius of the flight path curvature ρ_B (ρ_E) is:

$$\rho_B = \frac{\sqrt{2U}}{B} \cdot \sqrt{\frac{m}{q}} \tag{1.1}$$

$$\rho_E = \frac{2U}{E} \tag{1.2}$$

where U is the acceleration voltage.
Evidently, static electric fields cannot act as a mass separator but static magnetic fields can: the magnetic sector mass spectrometer is the textbook example of it.
The situation changes when using dynamic fields. Here an electric field can act as a mass separator as the ubiquitous quadrupole mass spectrometer illustrates. Another mass spectrometer working with variable fields – at least in the initial phase – is the Fourier-transform mass spectrometer (FTMS). FTMS is based on the ion-cyclotron resonance.
These three MS are mentioned briefly in the following section. In our work we were using time-of-flight mass spectrometers which will be described in details in the separate Section (1.2.2).

To compare differeut mass spectrometers one defines the mass resolution m/Δm, where m is the mass of a given ion and Δm the full-width at half

[7]The detection of singly charged human IgM with a molecular weight of almost 1 MDa has been reported [34].

Mass analyzer	Practical m/q limit	Mass resolution	Ionization techniques	Cost	MS/MS capabilities
Quadrupole	< 2000[a]	Low	ESI, FAB	Low	No
Time-of-flight	≫ 100'000	Low	MALDI, PD, (ESI)[b]	Low	No
Double-focusing sector	< 3000[c]	High	ESI, FAB	Moderate	No
Fourier transform MS	> 20'000[d]	High[e]	ESI, MALDI, FAB, (PD)[b]	Moderate	Yes

Table 1.1: Comparison of mass analyzers used for biopolymer analysis (reproduced from [36]).

The data in this table are representative of commonly equipped commercial instruments, not specialized research instrumentation. (1993)

a : Specially designed quadrupole rods with upper m/q limit of 4000 have become available.

b : This ionization technique has been demonstrated for these particular mass analyzers but is less commonly used than the other ionization methods.

c : This value is specified for full acceleration voltage; the mass range can be extended to approximately 10'000 at reduced acceleration voltages but with a concomitant loss in sensitivity[8].

d : This value is for a 7-T magnet; mass range scales with increasing magnetic field strength.

e : Resolution is mass dependent; ultrahigh resolution can be obtained at low mass, and high resolution is achievable for masses in the kilodalton region.

maximum (FWHM) of the corresponding peak in the mass spectrum.

Table 1.1 shows a comparison of mass analyzers used for biopolymer analysis.

1.2.1 Others than TOF mass analyzers

Magnetic sector instruments

The magnetic sector mass analyzer consists of a static magnetic field B perpendicular to the direction of the ion beam (see Figure 1.2). The mass determination (i.e. the mass to charge ratio) is given by

$$\frac{m}{q} = \frac{\rho^2 B^2}{2U} \tag{1.3}$$

where ρ is the radius of the curvature of the flight path and U the acceleration voltage (q·U is the kinetic energy of the ion).

[8]This statement of Buchanan and Hettich is certainly true for a magnetic sector coupled to a commonly used ion detector based on the secondary electron emission (e.g. secondary electron multiplier SEM) where the detection efficiency drops to low values for slowly moving ions (see Section 1.3.1), but it may not hold for cryogenic particle detectors since we could detect singly charged IgG ions (130 kDa) accelerated at only 3 kV with a detection efficiency of 100% (see Section 6.5 at page 79).

Usually U and ρ are hold constant while B is scanning the mass range.

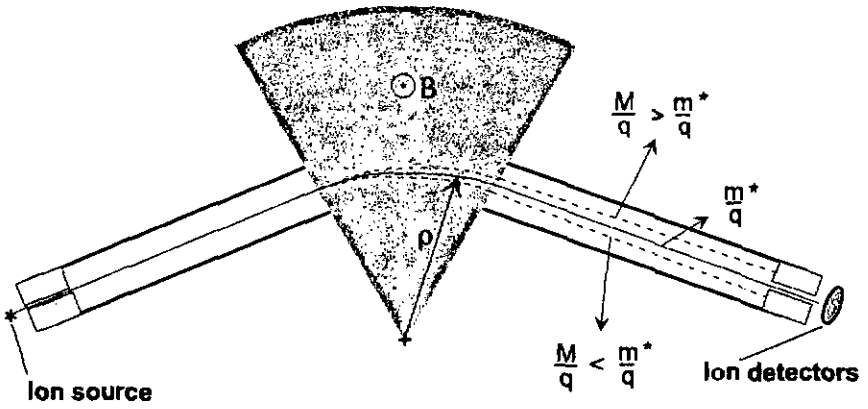

Figure 1.2: Single-focusing magnetic sector mass analyzer.

Since ion sources never produce absolutely mono-energetic ions, the mass resolution is limited. The trajectory differences due to kinetic energy fluctuations cannot sometimes he distinguished from the neighhouring m/q trajectories. This can be overcome with douhle-focusing devices which consist of an electric sector preconnected in series to a magnetic one. In the electric sector the energy dispersive properties are exploited (Equation 1.2).

Quadrupole mass analyzer

The quadrupole mass analyzer invented in 1953 by Paul and Steinwedel [37] acts as a mass filter, i.e. only one mass at the time can be determined. To get a full spectrum one has to scan through the mass range, which causes a decrease of sensitivity.

The hasic design is illustrated in Figure 1.3. The quadrupole mass analyzer consists of four hyperbolic rod electrodes which are in the most cases replaced by circular ones. A radiofrequency (RF) voltage V superimposed on a constant voltage U is applied to the electrodes forcing the entering ions

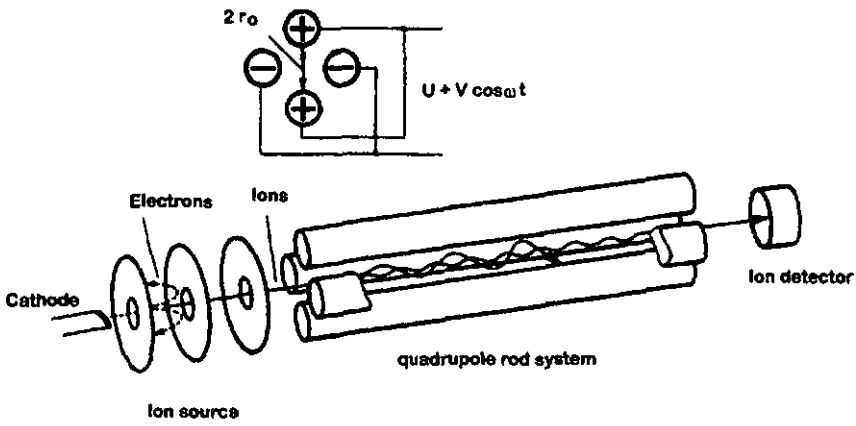

Figure 1.3: Schematic view of a quadrupole mass spectrometer. (Source: [38])

to a zigzag course. For a given U only the ions with the appropriate mass to charge ratio (m/q) move on a stable trajectory arriving at the ion detector. The others are deviated and finally pumped off.

Fourier-transform mass spectrometry

FTMS was introduced in 1974 by Comisarow and Marshall [39]. It is based on the cyclotron movement of a group of ions in the presence of a static magnetic field. The cyclotron frequency is given by

$$\nu = \frac{B}{2 \cdot \pi} \cdot \left(\frac{m}{q}\right)^{-1} \quad . \tag{1.4}$$

A pair of metal plates are registering the image current induced by the orbiting ion bundles. This signal has then to be Fourier-transformed to get the masses (frequency) and abundances (amplitude).

A pressure below 10^{-8} mbar has to reside in the FTMS cell, and a magnetic field of a few Tesla is needed to achieve good results for heavy molecules. FTMS is reviewed in [36].

1.2.2 Time-of-flight mass spectrometer

The principle of time-of-flight

The basic setup of the TOF mass spectrometer is shown in Figure 1.4. The ions are accelerated in a static electric field where all the ions acquire – in the simplest case – the same kinetic energy E:

$$E = \frac{1}{2} \cdot m \cdot v^2 = q \cdot U \ , \tag{1.5}$$

where q is the charge of the ion and U the acceleration high-voltage.
If the acceleration time is negligible compared to the time of flight t_{tof} (i.e. $d \ll L$), then one has $v = L/t_{tof}$. That leads to:

$$t_{tof} = \sqrt{\frac{1}{2} \cdot m \cdot \frac{L^2}{q \cdot U}} \ . \tag{1.6}$$

We therefore get the following important relations:

$$E \propto q \tag{1.7}$$

$$t_{tof} \propto \sqrt{\frac{m}{q}} \tag{1.8}$$

and

$$E \propto U \tag{1.9}$$

$$t_{tof} \propto 1/\sqrt{U} \tag{1.10}$$

More information about TOF MS can be found in [40].

1.2.3 Reflectron and delayed extraction

A major deficiency of TOF mass spectrometers is the limited mass resolution. In the case of MALDI TOF MS, it is mainly caused by the initial kinetic energy distribution of the ions, insufficiently fast electronics (including the detector) and ion collisions with the background gas. We will concentrate in this section on the first source of errors since the two others are solvable in a natural way.

The initial forward directed velocity of the ions causes an initial kinetic energy distribution δE which degrades the quality of the time-of-flight measurements as can be seen by substituting $(q \cdot U + \delta E)$ for $(q \cdot U)$ in Equation 1.6.

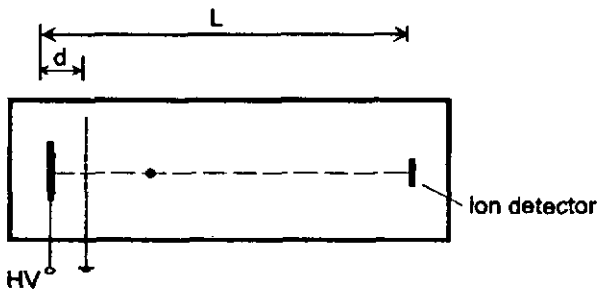

Figure 1.4: Schematic representation of the basic setup of a time-of-flight mass spectrometer. L is of the order of one metre and the acceleration voltage about 20 kV.

One remedy – the reflectron – was discovered by Mamyrin et al. in 1973 [41]. In the simplest case it is an ion mirror which reflects the ions back. The ions with a higher kinetic energy penetrate deeper into the retarding electrical field and hence have to travel longer en route to the ion detector. By carefully selecting the parameters of the reflectron it is possible to energy-focus the ion bundles and to improve the mass resolution.

Another way to improve the mass resolution is the delayed (or pulsed) extraction which was originally introduced by Wiley and McLaren in 1955 (time-lag focusing) [42][9]. Instead of working with a constant acceleration voltage the ions are allowed to be created in a field free environment. After a moment, the acceleration voltage is switched on. The more energetic ions travel somewhat further than the less energetic ones and are thus accelerated by a smaller electrostatic potential difference. An appropriate delay between the laser pulse and the turn-on of the acceleration voltage will energy focus the ions. Another advantage of delayed extraction is that the ion creation becomes softer; it is helpful to get good DNA results [43].

[9] *Delayed extraction*™ is a trademark of PerSeptive Biosystems, Inc.

1.3 Ion detectors

The ions separated according to their mass-to-charge ratio m/q have to be detected. The state-of-the-art detectors are the detectors based on the secondary electron emission followed by a secondary electron multiplication: microchannel plates are the most widely used ones. They are fast and have a large detector surface but suffer, as will be explained below in more details, from a severe decrease in detection efficiency for slowly moving massive ions. That is why other ion detectors have been developed having detection efficiencies less or not dependent on the ion mass: Faraday cup detectors [44, 45], inductive detectors [46] and cryogenic detectors. While the two first mentioned detectors need high ion currents to yield a signal above the noise level (in the best case 250 ions of the same m/q value), the cryogenic detectors are able to detect single macromolecule impacts with a 100% detection efficiency which is independent of the mass and charge state of the incoming particle. Even neutral molecules are indifferently detected since the detection mechanism relies on a calorimetric detection scheme.

1.3.1 State-of-the-art ion detectors

Secondary Electron Multipliers (SEM) are quite similar to the well known photomultipliers (PM). The ion hitting the first dynode (ion converter, photocathode) creates a number of electrons by secondary electron emission. These electrons are then accelerated from one to another dynode creating additional secondary electrons. This avalanche process leads to a high current gain from 10^4 to 10^8.

Microchannel Plates (**MCP**) and Single Channel Electron Multipliers (Channeltron©) are similar to the SEM: the discrete dynodes are replaced by a continuous one made out of a coated glass tube [47]. While the Channeltron consists of one single glass tube, the Microchannel plate is constituted of 10^4 to 10^7 channels (see Figure 1.5).

They are often mounted in the so called Chevron configuration, a dual channel plate configuration as shown in Figure 1.6, to increase the overall gain ($\approx 10^7$). These detectors are very fast, a time resolution below 1 ns is possible [48], and the detector surface is large.

One problem encountered with MCP detectors is saturation. The dead time of a channel is about 20 ms [48] causing considerable sensitivity problems in the presence of a strong matrix signal. Pulsed deflection plates kicking off the light matrix ions cannot completely clear the situation since reneutralized ions are quite abundant as well [45].

Aging is another problem. All detectors based on the secondary electron multiplication suffer from a decrease in sensitivity with time, especially when

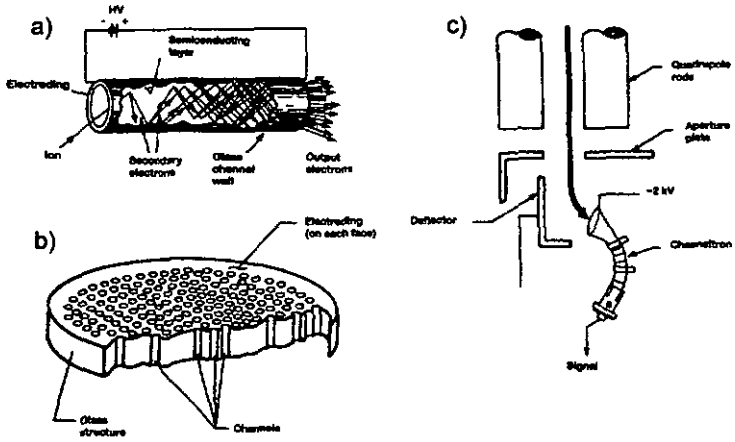

Figure 1.5: Detectors based on the secondary electron emission.
a) Continuous dynode of channel electron multiplier (reproduced from [49]).
b) Microchannel plate (from [50] in [51]).
c) Channeltron coupled to a quadrupole mass spectrometer (from [47]).

run in a vacuum which is not excellent as is quite often the case in MALDI TOF mass spectrometers.

But all these problems are negligible compared to the fact that the detection efficiency becomes very low for ions moving slower than 10^4 m/s [52, 45]. This velocity threshold corresponds to a singly charged ion of 38 kDa accelerated through a 20 kV potential difference. Ions with a higher mass are less effectively detected but to which extent is still debated [53, 54, 55, 56].

Higher masses can be measured by increasing the acceleration voltage, but the onset of uncontrolled discharges gives a practical limit of about 30-40 kV. Another way to increase the sensitivity is to post-accelerate the primary ions onto a conversion dynode. The emitted secondary ions and electrons are then detected with one of the above mentioned detectors. But the time needed for the secondary ions to travel from the conversion dynode to the detector compromises the time and hence mass resolution.

Furthermore, MALDI-born ions tend to decay in the flight tube en route to the ion detector (while barely any fragmentation from the desorption process can be observed). So after the initial acceleration the flight tube should be kept field free to avoid spread in flight times of neutrals, parent and fragment ions degrading the mass resolution [57].

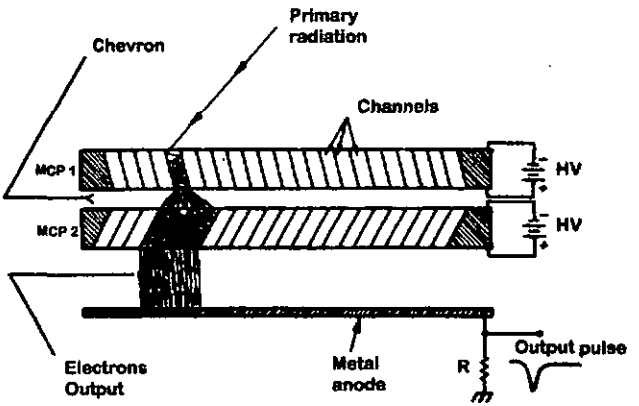

Figure 1.6: Chevron operation of MCPs (reproduced from [48]).

1.3.2 Cryogenic particle detector

The use of cryogenic particle detectors as high-efficient (ion[10]) detectors of massive macromolecules was proposed in 1995 by Twerenbold [1]. The cryogenic detectors themselves will be presented in Chapter 2. Here we only review the results obtained by the three collaborations which have been working by now in this field of research.

The Neuchâtel/GMU/PSI collaboration was the first one which succeeded in detecting macromolecule impacts, see Chapter 4 and [2]. We could prove that it is indeed possible to detect *single* massive macromolecule impacts with a cryogenic detector (SIS tin junction). Spectra of proteins and DNA-oligonucleotides with up to 120 bases have been recorded, see Chapter 6 and [4].

The LLNL/LBNL/Conductus[11] collaboration confirmed somewhat later our protein results [58, 59, 60]. In addition, by comparing the count rates and spectra obtained by their SIS niobium tunnel junctions and a multichannel plate, they found that the detection efficiency for their cryogenic detector is two to three orders of magnitude higher per unit detector area (for HSA,

[10]The particle has not to be charged in order to be detected by a cryogenic particle detector.

[11]LLNL: Lawrence Livermore National Laboratory, CA, USA. LBNL: Lawrence Berkeley National Laboratory, CA, USA and Conductus Inc., Sunnyvale, CA, USA.

66 kDa at 25 kV acceleration voltage).

The NIST/Neuchâtel/GMU collaboration was working with a hot-electron microcalorimeter operated at 100 mK. It was clearly shown that cryogenic particle detectors can determine the charge state of the molecular ions, see Chapter 5 and [3, 5].

1.4 Our mass spectrometer

A mass spectrometer is composed of an ion source, a mass analyzer and an ion detector. Natural combinations of ion sources and mass analyzers are MALDI–TOF, ESI–quadrupole and ESI–sector.

Quadrupole and magnetic sector mass analyzers are actually stigmatized with a m/q limit of a few thousands. Thus high mass molecules can be measured only when the ions are highly charged as with an ESI ion source. But ion charge states of, let us say, 200 entails the impossibility of investigating the charge separation capability of cryogenic detectors.

We chose to work with a MALDI-TOF MS. MALDI produces mainly singly and doubly charged ions which fits well with our wish to prove the charge discrimination capability of cryogenic detectors. MALDI-TOF mass spectrometers can be home-built at low cost and the preparation of MALDI-probes is straightforward.

Of course, a cryogenic particle detector has been chosen to work with. From the choice of possible candidates (see Chapter 2) the superconducting tunnel junctions (STJ), where both superconducting films are of tin, have been selected. This mainly, because we owned already the know-how to fabricate this devices.

Chapter 2

Cryogenic particle detectors

In the first section of this chapter we will show how to reach low temperatures and why cryogenic detectors have been so much investigated by now. In the second section we will review the essentials of superconductivity, and, finally, in the last section some cryogenic particle detectors will be presented.

2.1 Generalities

A cryogenic particle detector is a detector operated at low temperatures, i.e. at 4.2 K[1] or below. 4.2 K is the temperature of liquid ^{4}He (L^4He) at atmospheric pressure; when pumping on the L^4He bath one can cool the liquid down to 1.2 K. Similarly, using the rare isotope ^{3}He, 0.3 K are reachable. This temperature range is readily attainable as long as liquid nitrogen LN_2 (77 K) and a L^4He provider is around. If one has to go to lower temperatures, some considerable technical effort has to be undertaken: with an adiabatic demagnetization refrigerator (ADR) 50 mK are achievable, with a dilution refrigerator $\leq$ 10 mK. It is possible to work in the sub-millikelvin region but the low temperature detectors community has never been using such temperatures. More details concerning cryogenic techniques can be found in [62, 63, 64, 65].

Why to work at low temperatures:

1. The influence of the thermal phonon population becomes negligible compared to the excess phonons produced by the impact of a particle (see Fig. 2.9, page 34).

[1] The absolute zero is 0 K (Kelvin). It corresponds to -273.15 °C.

2. New solid state physics phenomena appear, like superconductivity or superfluidity.

Three reasons why cryogenic detectors have been investigated by now:

1. **High energy resolution.** Because of the low mean energy ϵ required to create a single detectable excitation, cryogenic particle detectors used in a proper way are high energy resolution detectors. The gap of a superconductor – half the energy necessary to break up a Cooper pair – is about 1 meV leading to a tiny ϵ of a few meV. This is to be compared to the few eV required to create an electron-hole pair in a semiconductor, to the $\approx$15 eV to ionize a gas molecule of a gaseous detector or even to the $\approx$100 eV for a scintillator [51]. The energy of a thermal phonon at 0.5 K is smaller than 0.5 meV thus an appropriate phonon sensor will be able to detect excess phonons produced by the impact of a particle with high sensitivity.

   But high energy resolution is of moderate importance for the detection of macromolecules.

2. **High detection efficiency for poorly- and non-ionizing particle interactions.** It is known that cold dark matter (CDM) in a form of weakly-interacting massive particles (WIMPs) may interact elastically with the nucleus in a target and that the energy deposition will be by the recoiled nucleus. This process is poorly ionizing due to the mass mismatch between recoiling nucleus and target electron [66]; most of the energy is deposited as phonons which are only detectable with a cryogenic particle detector. That is the reason why several cryogenic dark matter detectors have been built in the last years.

   Since the impact of a massive macromolecule is also poorly ionizing, one can expect a substantial improvement of the detection efficiency when using cryogenic detectors.

3. **The wide choice of materials available** for building these detectors compared to the rather restricted variety of usable semiconductors, scintillators and gases. Almost every isotope can be investigated; e.g. the University of Milano group could lower the neutrinoless double beta decay lifetime of ^{130}Te by three orders of magnitude using a 73.1 g $^{130}Te\,O_2$ crystal as bolometric absorber [67].

   This feature is of little importance for detecting macromolecules.

2.2 Superconductivity

Let us first recall the basic concept of the Fermi sphere. Electrons are spin-1/2 particles and have hence to follow the Fermi-Dirac statistic based on the Pauli principle. At zero temperature, the energy levels are filled with two electrons with opposite spins up to the Fermi energy E_F ($\approx 5\,eV$). The occupied states are forming the Fermi sphere (in momentum space), see Figure 2.1. The highest velocity of a conduction electron at zero temperature is the Fermi velocity v_F of $10^6\,m/s$ ($\approx c/100$!).

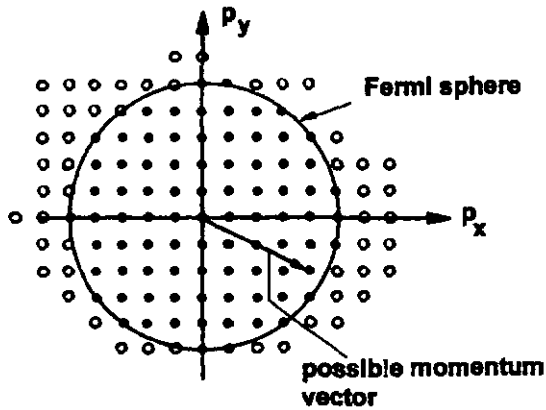

Figure 2.1: Illustration of a center plane of the Fermi sphere showing the allowed states for the conduction electrons. The full circles represent occupied states and the open circles empty states. The surface of the Fermi sphere – the Fermi surface – separates the occupied from the unoccupied levels. (After [68])

When a metal is cooled down, its resistivity decreases because the thermal phonon population freezes out so that the resistance part due to electron-phonon scattering vanishes. The resistivity of normal metals reaches a limit at the so-called residual resistance which is caused by impurity and defect scattering (see Fig. 2.2), but some elements and alloys undergo a dramatic change which was first discovered by Heike Kamerlingh Onnes: the **DC-resistance drops abruptly to zero** at a certain critical temperature T_c [69] (see Fig. 2.2). He called this new state superconductive state [70]. In

Table 2.1 values of critical temperatures of some commonly used superconductors are listed.

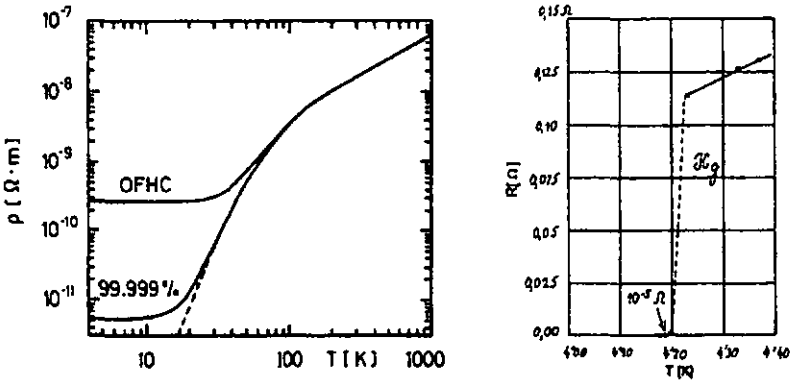

Figure 2.2: Left: the residual resistance of OFHC copper and 99.999% pure annealed copper. The dashed line represents the calculated case of a impurity and lattice defect free copper sample.
Right: the first measurements of superconductivity by Kamerlingh Onnes. (Figures reproduced from [68])

Meissner and Ochsenfeld could show in 1933 that **superconductors are also perfectly diamagnetic** [71]: they expel entirely magnetic fields[2]. This property is an independent phenomenon which cannot be explained by the onset of zero-resistance.

An important discovery which helped significantly to understand superconductivity was the **isotope effect**. Almost at the same time in 1950, two independent groups found, that the superconducting transition temperature T_c of mercury depends with one over the square-root of the isotope mass m of the lattice nuclei [72, 73]: $T_c \propto m^{-1/2}$. This measurements confirmed that phonons have to be included in a microscopic theory of superconductivity.

[2]for fields lower than H_c for type-I superconductors and H_{c1} for type-II ones (see page 29). Since the magnetic field has to decrease continuously to zero, it will penetrate somewhat at the surface (see page 28: London penetration depth λ_L)

Element	T_c [K]	H_c [Gauss]	θ_D [K]	Type
Al	1.20	99	420	I
In	3.40	293	109	I
Nb	9.26	1980	240	II
Pb	7.19	803	96	I
Sn	3.72	305	195	I
Ta	4.48	830	260	I

Table 2.1: Critical temperatures, critical fields and Debye temperatures of some commonly used superconductors. The values for T_c and H_c are quoted by [74], the values for θ_D from [75].

2.2.1 The BCS theory of superconductivity

J. Bardeen, L.N. Cooper and J.R. Schrieffer proposed in 1957 their microscopic model of superconductivity which is known as the BCS-theory [76]. According to this successful model, the electrons of a superconducting metal undergo a pairing when $T < T_c$: two electrons at a time with opposite wave vectors $\vec{k}$, $-\vec{k}$ and spins are binding together forming the so-called Cooper pairs. The coupling interaction is mediated via virtual phonons.

Since the highest possible phonon energy is given by the Debye energy $k_B \cdot \theta_D \doteq \hbar \cdot \omega_D \approx 10\,\mathrm{meV}$, only a fraction of the conduction electrons can participate: those in a shell of thickness $\pm k_B \cdot \theta_D$ around the Fermi surface. But one has to bear in mind that the inner (not paired) electrons do not contribute to normal conduction either ($k_B \cdot \theta_D \gg k_B \cdot T_c$).

The small net attractive force causes a rather extended spatial extension of the Cooper pairs called coherence length ξ. Since ξ is of the order of 1000 Å, millions of other pairs are between each others showing that they should not be imagined as siamese twins.

All the Cooper pairs are in the same quantum state explaining the zero DC-resistivity of superconductors.

There are no excited states of Cooper pairs. An input of an energy higher than $2 \cdot \Delta$ (twice the gap; see below) will break them up into single electrons called quasiparticles (qp).

The BCS theory is able to predict many quantitative equilibrium properties [74]:

Critical temperature T_c

$$k_B \cdot T_c = 1.13 \cdot \hbar \cdot \omega_D \cdot e^{-1/N_0 V_0}$$

where N_0 is the density of states in the normal state at the Fermi energy, $\hbar \cdot \omega_D$ is the Debye energy and V_0 is the interaction potential of the Cooper pairs.

Energy gap Δ

The BCS ground state is characterized by a ground state energy which is separated from the levels of quasiparticles (qp) by a energy gap Δ.

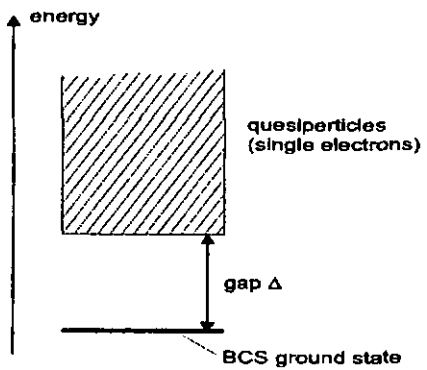

Figure 2.3: The energy gap separating the BCS ground state from the quasiparticle levels.

For the energy gap at zero temperature we have:

$$\begin{aligned} \Delta(0) &= 2\hbar \cdot \omega_D \cdot e^{-1/N_0 \cdot V_0} \\ &= 1.76\, k_B \cdot T_c \end{aligned} \tag{2.1}$$

The gaps' temperature dependence is given by:

$$\frac{\Delta(T)}{\Delta(0)} = 1.74 \left(1 - \frac{T}{T_c}\right)^{1/2} .$$

Specific heat

There is a discontinuity in the specific heat at T_c, see Figure 2.4. The difference of the specific heat in the superconductive state c_s and in the normal one c_n (driven normal by a magnetic field) is:

$$\left.\frac{c_s - c_n}{c_n}\right|_{T_c} = 1.43\,.$$

But at low temperatures c_s is becoming much smaller than c_n as can be seen in Fig. 2.4:

$$c_s = 1.34\gamma \cdot T_c \left(\frac{\Delta(0)}{T}\right)^{3/2} \cdot e^{-\Delta(0)/T} + B \cdot T^3.$$

The first term is due to the electronic contribution to the specific heat, the second is caused by the phonons; γ is the coefficient of the linear term in the specific heat of the metal in the normal state.

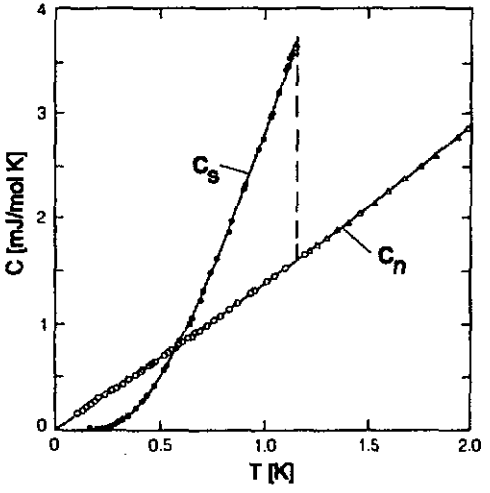

Figure 2.4: The specific heat of aluminium in the superconductive state (c_s) and in the normal state (c_n)(driven normal by a magnetic field of 300 Gauss). (From [62])

Coherence length ξ

The coherence length is a measure of the size of a Cooper pair. It can be evaluated from the Heisenberg uncertainty relation:

$$\xi_0 \equiv \Delta x = \frac{\hbar}{\Delta p} \cong \frac{\hbar \cdot v_F}{2 \cdot \Delta} ,$$

by assigning the uncertainty Δx to the coherence length ξ_0 at zero temperature. The temperature dependence is given by

$$\xi(T) = \xi_0 \left(1 - \frac{T}{T_c}\right)^{-1/2} .$$

The finite value of ξ causes the Cooper pair density to decrease smoothly at the end of the superconductor, see Figure 2.5.

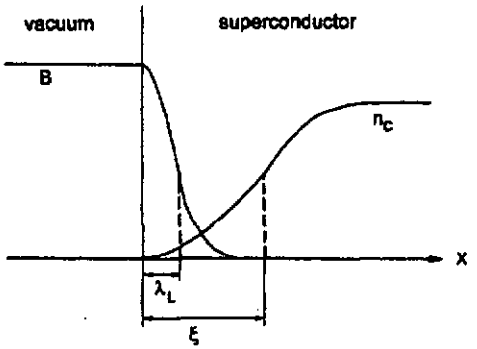

Figure 2.5: The coherence length ξ and the London penetration depth λ_L at the vacuum-superconductor boundary.

London penetration depth λ_L

The Meissner-Ochsenfeld effect states that there is no magnetic field in a superconductor – it is true for the bulk at low enough temperatures. At the surface the magnetic field penetrates slightly (see Figure 2.5); the exponential attenuation length is given by the London penetration depth λ_L which is of the order of 30 nm. The temperature dependence calculated with the BCS theory gives [75]:

$$\lambda_L \propto \left(1 - \frac{T}{T_c}\right)^{-\frac{1}{2}}$$

$$\lambda_L \to \infty \quad \text{for} \quad T \to T_c .$$

Critical fields B_c

The Ginzburg-Landau parameter $\kappa \doteq \lambda_L/\xi$ defines if a superconductor is a type I or type II one:

$$\begin{aligned} \text{type I} &: \kappa < 2^{-1/2} \\ \text{type II} &: \kappa > 2^{-1/2} \ . \end{aligned}$$

For a *type I superconductor, the magnetic fields are repelled for fields* below H_c (Meissner phase) and beyond H_c the superconductive state vanishes (normal phase) (see Figure 2.6). For type II superconductors the situation is more complex: below H_{c1} the magnetic field is repelled, hetween H_{c1} and H_{c2} a mixed phase is where fluxoids can bore through the superconductive phase. Above H_{c2} the superconductivity vanishes.

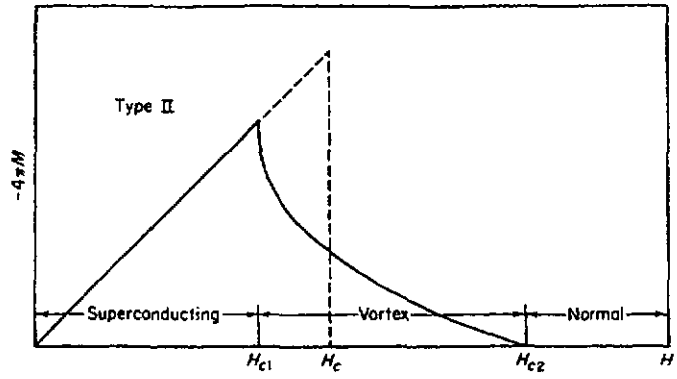

Figure 2.6: Magnetisation of type II superconductor (full line) and type I (dashed line) superconductors. (Source: [103])

Some numerical values for tin [68, 103]:

Tin is a superconductor which is well described by the BCS model.

1. Type I
2. $T_c = 3.7\,K$

3. $\xi \approx 200\,\mathrm{nm}$

4. $H_c = 305$ Gauss

5. $\lambda_L \approx 30\,\mathrm{nm}$

2.3 Cryogenic particle detectors

In the past ten, twenty years numerous low temperature detectors have been built and improved in a way that impressive performances were achieved. The major applications are X-ray spectroscopy and detection of rare events (neutrinos, dark matter).

To be of benefit in the field of biopolymer mass spectrometry the cryogenic detector has to be fast and robust. Since macromolecules react on the surface no thick absorber is necessary.

This section is organized as follows: first we present bolometers and their thermistors. These detectors measure the temperature rise of an absorber caused by the impact of a particle. This part is concluded with a short introduction to the transition edge sensors. Then superconducting tunnel junctions are discussed and finally the third part is dedicated to the hot-electron microcalorimeter.

More information about cryogenic particle detectors can be found in [77, 78] and in the proceedings of the 'Low Temperature Detectors' Workshops [79]-[85].

2.3.1 Bolometers

The working principle of bolometers is simple: the particles interact in the absorber leaving a certain amount of energy E which will rise the temperature (ΔT) of the absorber. A temperature sensor measures ΔT (see Figure 2.7). A naïve model gives:

$$\Delta T = \frac{E}{C(T)} \cdot e^{-t/\tau} \quad , \quad \tau = \frac{C(T)}{G(T)} \quad ,$$

where C(T) is the heat capacity of the absorber and G(T) the thermal conductance of the link between the absorber and the cold plate at base temperature T_0.

At low temperatures the heat capacity of metals is dominated by the contribution of the conduction electrons while for dielectric (semiconductor

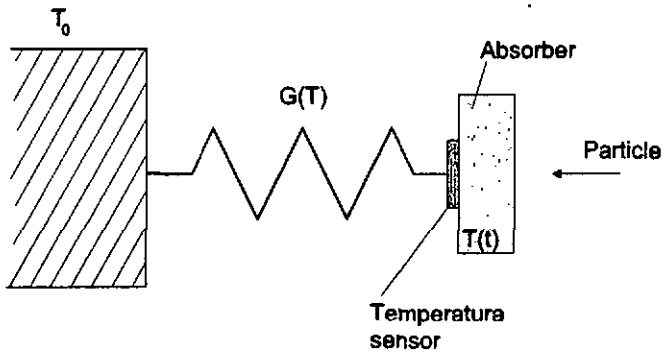

Figure 2.7: Scheme of a bolometer.

at low temperature) and superconducting absorbers the phonon (lattice vibrations) contribution is leading:

$$\begin{array}{lcll} \text{dielectric} & : C(T) & = A \cdot \left(\frac{T}{\theta_D}\right)^3 & \propto T^3 \\ \text{metal} & : C_m(T) & = \gamma \cdot T + A \cdot \left(\frac{T}{\theta_D}\right)^3 & \propto T \\ \text{superconductor} & : C_s(T) & = B \cdot e^{-b \cdot T_c/T} + A \cdot \left(\frac{T}{\theta_D}\right)^3 & \propto T^3 \ , \end{array}$$

where A = 1944 J/(mol K), B, b and γ are constants, θ_D is the Debye temperature and T_c the critical temperature of the superconductor.

Although dielectric and superconducting absorbers are chosen in most cases in order to have large signals, thin metal absorbers can also be used – the hot-electron microcalorimeter used in our collaboration with NIST and GMU is an example of it (see Sections 2.3.3 and 3.3.2).

Temperature sensors

As temperature sensors either doped semiconductor thermistors (directly implated dopants in silicon absorbers or neutron transmutation doped (NTP) germanium thermistor chips which have to be glued onto the absorber) or transition edge sensors (TES) – sometimes also called superconducting phase-transition (SPT) thermometers – are used.

A TES is a thin superconducting film evaporated on the absorber. Since the normal-to-superconductor transition is very sharp, the temperature dependence of the resistance of this film is steep resulting in a very sensitive temperature sensor. Combined with the electrothermal feedback (ETF)

[86, 95] which assures a stable operating point, much faster response time (μs) and a better energy resolution it is becoming an important tool in the field of cryogenic detectors.

Generally, to built fast detectors one has to assure fast thermal relaxation, i.e. high thermal conductivity. According to the Wiedemann-Franz law this turns out to use low impedance devices. So a TES is promising to be faster than a doped semiconductor thermistor.

Furthermore, if one would detect immediately nonthermal phonons instead of awaiting the deposited energy to be thermalized, a considerably faster detector can be built. Twerenbold proposed a **TES based macromolecule detector** [87], see Figure 2.8. The TES is operated at a temperature slightly below the critical temperature T_c of the film. A macromolecule hitting the detector will drive a portion of the superconducting meander film normal resulting in a measurable voltage drop accross the TES.

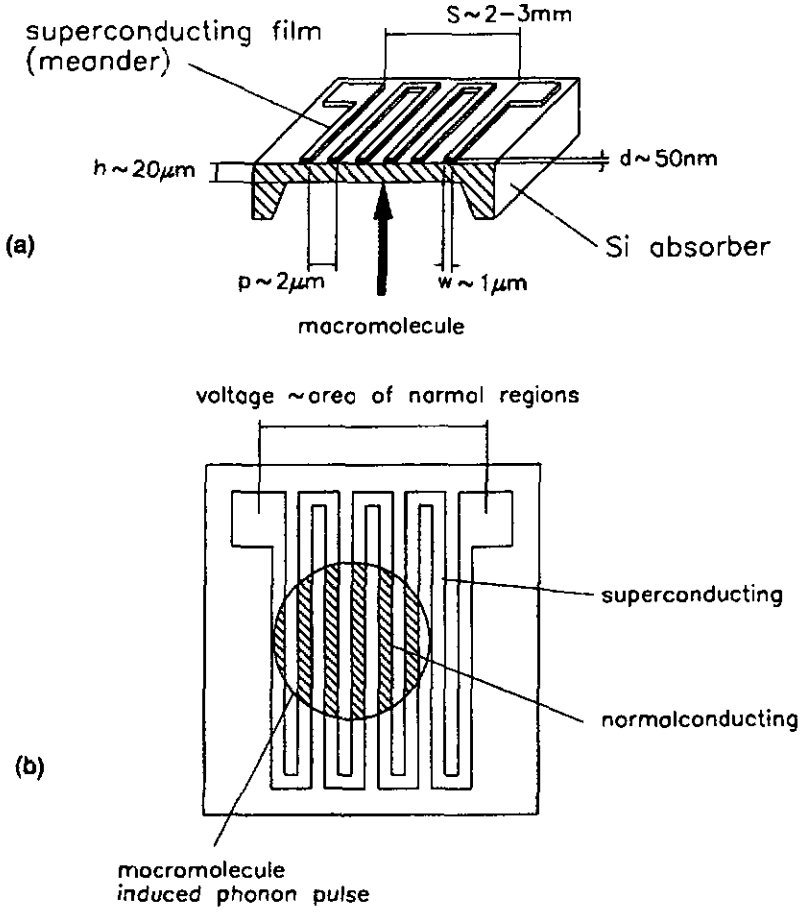

Figure 2.8: Proposed transition edge sensor based macromolecule detector. (Source: [87])

2.3.2 Superconducting tunnel junctions

A superconducting tunnel junction (STJ) consists of two superconducting thin films separated by a thin insulating barrier – the tunnel barrier – of a thickness of 1-2 nm. STJs measure the number of excess quasiparticles (qp) produced by the impact of an incident particle. A particle interacting in a superconductor creates nonequilibrium phonons as well as excess quasiparticles. These two excitations are coupled together since a phonon with an energy higher than $2 \cdot \Delta$ can break up a Cooper pair and two qp recombining together release a phonon.

So in order to run a STJ well, low temperatures are required to freeze out the thermal phonon population which can create thermal qp causing qp recombination. As a rule of thumb, a temperature of the order of $T_c/10$ is necessary (see Figure 2.9).

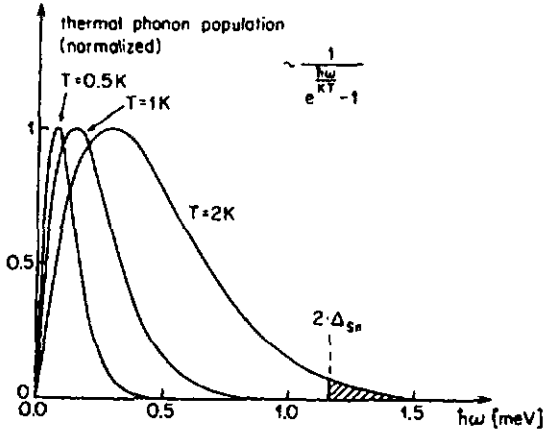

Figure 2.9: The normalized thermal phonon population for three temperatures. $2 \cdot \Delta_{Sn}$ is the threshold energy to break a Cooper pair in tin. (Source: [88])

Since the energy of an incoming particle is typically a few keV – much higher than the Debye energy of the absorber (e.g. Si: 54 meV) – , all phonon modes are initially excited (Figure 2.10 shows the phonon density of states in silicon). These high-frequency phonons deexcite quickly so that after $\approx$ 100 ps a substantial part of the energy is stored in excess qp near the band gap.

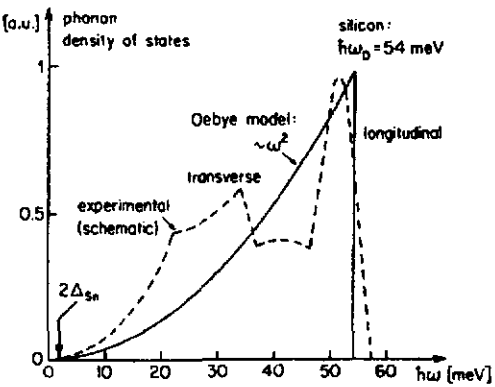

Figure 2.10: The phonon density of states in silicon. $2\Delta_{Sn}$ is the threshold energy to break a Cooper pair in tin. (Reproduced from [88])

It is also possible to detect particles hitting the substrate near the junction since (ballistic) energetic phonons can reach the junction and break up Cooper pairs. These indirect hits are called substrate or phonon pulses.

It is now important to collect these excess quasiparticles before they recombine or get lost by qp diffusion out of the junction. By biasing the junction and applying an appropriate magnetic field in the detector plane to suppres the Josephson supercurrent (tunneling of Cooper pairs; DC Josephson effect) (see Fig. 2.11), the qp density can be measured by quantum mechanical tunneling. The collected charge can be described by [89, 90]:

$$Q_{eff} = \frac{E}{\Delta} \cdot \frac{\tau_{tun}^{-1}}{\tau_{tun}^{-1} + \tau_R^{-1} + \tau_x^{-1}} \ ,$$

where E is the deposited energy by the particle, $\tau_{\rm tun}$ is the tunneling time, $\tau_{\rm R}$ the recombination time and $\tau_{\rm x}$ stands for phonon losses to the substrate and the qp diffusion.

We have [89, 90]:

$$\begin{aligned} \tau_{tun}^{-1} &\propto (R_N \cdot A)^{-1} \propto \sigma \\ \tau_R^{-1} &\propto \sqrt{T} \cdot e^{-\Delta/k_B \cdot T} \ , \end{aligned}$$

where R_N is the normal resistance of the tunnel junction, A is the overlap area of the junction and σ is the electrical conductivity of the junction.

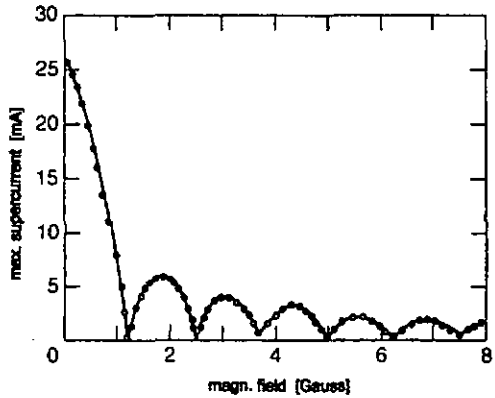

Figure 2.11: Fraunhofer pattern of the peak Josephson supercurrent in function of the applied magnetic field for a Sn/Sn-ox/Sn tunnel junction. (After [75])

To get large signals it is necessary to work at low temperatures ($T/T_c \simeq 0.1$) to minimize qp recombination and to design the geometry of the junctions in a way to reduce qp diffusion (see Section 3.3.3, page 52). More information about the nonequilibrium model of STJs can be found in [89, 90].

An interesting fact is that whether the particle hits the film 1 or 2, the signal has the same sign (see Fig. 2.12). Their pulse shapes, however, differ resulting in peak doubling in the pulse height spectrum (see Fig.3.13 at page 57).

Figure 2.13 shows a schematical current-voltage characteristic of a tin SIS tunnel junction. The current for voltages below Δ/e is due to thermally excited qp. The current rise for higher voltages is caused by the simultaneous tunneling of two quasiparticles (two qp, not one Cooper pair). At the voltage $2\Delta/e$ the superconductors are driven normal; the ohmic slope (R_N^{-1}) is given by the normal electron tunneling.

STJ are usually biased slightly below Δ/e. When using a FET based preamplifier, the dynamic resistance ($R_D \doteq \partial U/\partial I$) at the operating point should be high (at least a few kΩ) to match to the impedance of the FET. The

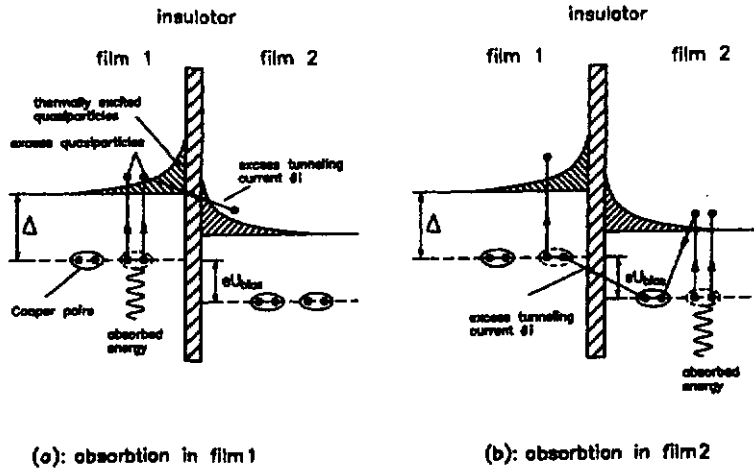

Figure 2.12: (a) shows the situation were the absorption took place in the film 1; in an intuitive way the excess tunneling current flows in the direction of decreasing energy potential. The situation in (b) is more complex, where a quasiparticle is broken up in the film 2 at lower energy potential. In recombining one qp of film 2 with an another one from film 1 we have the excess tunneling current flowing again from left to right. (From [77])

normal resistance (R_N) on the other hand should be small to allow tunneling.

A typical area of a STJ is of the order of $100 \times 100\ \mu m^2$; it is not possible to make junctions much bigger. Increasing the overlap area entails that the junction capacitance increases and the dynamical resistance R_D diminishes resulting in a degraded signal-to-noise ratio [91].

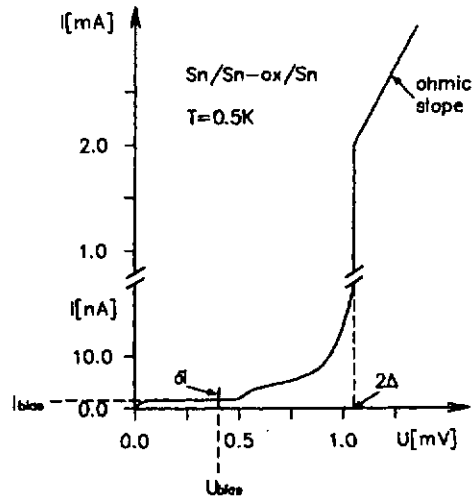

Figure 2.13: A schematical current-voltage characteristic for a Sn/Sn-ox/Sn tunnel junction. Indicated is the usual operating point (U_{bias}, I_{bias}). δi represents the excess tunneling current caused by the impact of a particle. (From [77])

2.3.3 Hot-electron microcalorimeter

The hot-electron microcalorimeters belong together with the electrothermal feedback transition edge sensors (ETF-TES) to the fast thermal detectors. They consist of a thin (normal) metal film acting as absorber and a device to measure the electron temperature rise [92, 93].

The **metal absorber** has to be cooled to rather low temperatures ($\approx$100 mK) in order that its heat capacity is small and the phonons and electrons are decoupled. Since at such temperatures the electronic heat capacity C_e dominates over the phonon contribution, most of the deposited energy E goes to the electrons resulting in an increased electron temperature. Hence the name 'hot electron microcalorimeter' or 'hot electron bolometer'. From the rapid thermalization of the energy and the small absorber volume one can infer that the electron temperature rise is given by $\Delta T = E/C_e$.

Usually a NIS tunnel junction is used to measure the electron temperature rise, although also ETF-TES have been investigated [95].

In Figure 2.14 a scheme of such a device is shown. It is a similar one we used in our collaboration with NIST and GMU, see Section 3.3.2 and Chapter 5. The silver absorber is evaporated on a Si_3N_4 membrane to reduce phonon losses to the substrate. The electron temperature rise is measured with an NIS tunnel junction (Ag-absorber/Al-ox/Al). The big silver pad near the superconducting electrode of the junction acts as thermalizer of the power produced by the quasiparticle recombination[3]. A NIS junction is best preamplified with a SQUID since the dynamic resistance is low.

In a **NIS tunnel junction** there is no net charge tunneling from the superconductor to the normalconductor side: the creation of a quasiparticle leaves an empty state – a quasihole –, which tunnels as well as the quasiparticle to the normal side (see Figure 2.15).

The tunneling current is mainly dependent on the electron temperature at the normalconducting side and is flowing from the normal to the superconductor side. The junction is biased with a constant voltage U_{bias} such that $\Delta - e \cdot U_{bias} > k_B \cdot T$, so that only the 'hot' electrons do tunnel (see Figure 2.16). The tunneling of less energetic electrons and of holes (empty states below the Fermi level) is prohibited by the gap in the superconductor density of states.

[3]NIS junctions behave like refrigerators: they remove energetic 'hot' electrons from the normal side to the superconductor side where they recombine emitting phonons, i.e. release heat [96]. The tunneled hot electrons are replaced by electrons at the Fermi level. Nahums' group is developing an all-electronic on-chip refrigerator based on the NIS tunnel junction reaching 100 mK from a 300 mK bath.

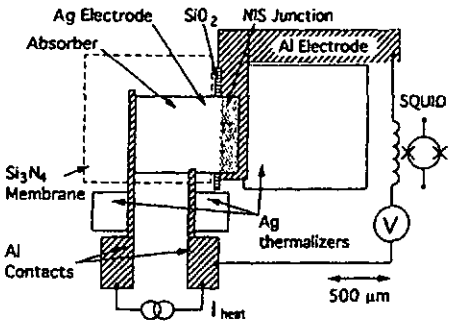

Figure 2.14: Scheme of a hot electron microcalorimeter, a NIS tunnel junction where the metal electrode absorbs the energy of the particles and the junction measures the increased electron temperature. (After [93])

No Helmholtz coil is necessary since there is no Josephson supercurrent flowing in NIS junctions.

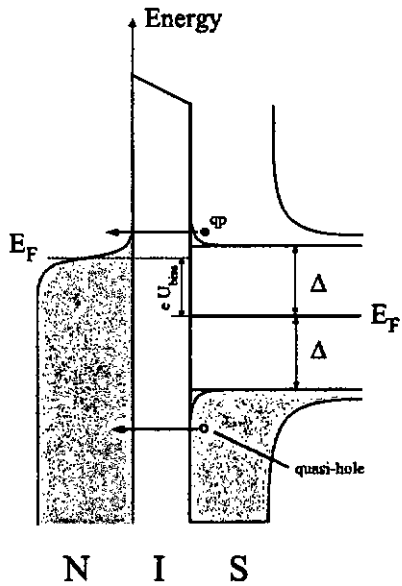

Figure 2.15: The density of states diagram of a NIS tunnel junction showing that there is no net charge tunneling from the superconductor to the normal side.

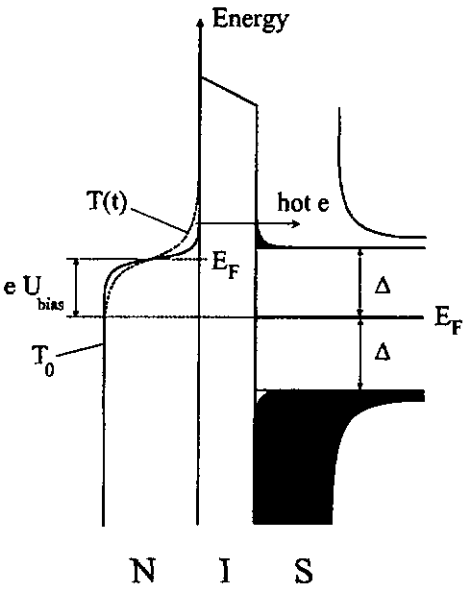

Figure 2.16: NIS tunnel junction. The full line shows the occupied electron states at the base temperature T_0 and the dashed line for the transient situation of increased electron temperature T(t) after a particle impact. The junction is biased in a way that only hot electrons can tunnel.

Chapter 3

Biopolymer sample preparation and instrumentation

3.1 Sample preparation

The following products have been used:

- Macromolecules:
  - Anti-mouse immunoglobulin **IgG**, whole molecule, developed in goat, molecular weight: 130'000 Da, Sigma Immuno Chemicals M-8642.
  - Bovine Serum Albumin (ac-**BSA**), acetylated, molecular weight: 66'430 Da, Sigma B-2516.
  - **Lysozyme** (Muramidase) from hen egg white, molecular weight: 14'300 Da, Boehringer Mannheim # 107255.
  - 40-mer **oligonucleotides**, GibcoBRL (Life Technologies) NIH Cust Po # BAK 100694A
  - 40-mer[1], 70-mer[2] and 120-mer[3] **oligomers**; Mycrosynth AG, Balgach, Switzerland.

[1] ttt tat tga ttg att gat tga ttg att gat tga ttg ttt t; molecular weight: 12339 Da

[2] att gat tga ttg att gat tga ttg att gat tgt ttt att gat tga ttg att gat tga ttg att gat tgg g; molecular weight: 21757 Da

[3] 5'-att gat tga ttg att gat tga ttg att gat tgt ttt att gat tga ttg att gat tga ttg ttg att gtt tta ttg att gat tga ttg att gat tga ttg att gtt tta tta gat tgg ggg-3'; molecular weight: 37 kDa.

- Matrix:
  - Sinapinic acid $C_{11}H_{12}O_5$: 224 Da, Fluka 85430.
  - 3-Hydroxypicolinic acid **3-HPA**: 139 Da, 98%, Aldrich 15'230-7.
- Solvents and others:
  - Water for chromatography, Merck. Subsequently called water.
  - Ethanol absolute GR, pro analysis, Merck.
  - Trifluoroacetic acid **TFA**, 99+%, suitable for protein sequencing, Aldrich 29,953-7. This pure acid is diluted in water to a concentration of 0.1%.
  - Acetonitrile **ACN**, 99.9%, HPLC grade, Sigma-Aldrich 27,071-7.

The recipe used in most cases for the protein samples :

- **Matrix**: 100 mg of the sinapinic acid powder is dissolved in 6 ml of ethanol and 4 ml of water.
- The **macromolecule** powders are dissolved in 0.1% TFA: respectively 1 mg of lysozyme, IgG or BSA in 1 ml.
- **MALDI-probe**: 20 μl of the sinapinic acid solution and 20 μl of one of the macromolecule solutions are mixed together, vortex-stirred and then dripped on a sample holder[4]. This mixture is let to be dried in air under an infrared lamp. Steady stirring the mixture with a glass rod produces a rather homogeneous polycrystalline sample as can be seen on the following SEM[5]-pictures.

The recipe for oligomer MALDI probes:

The matrix solution is obtained by dissolving 3-HPA powder in 50% aqueous acetonitrile; the analyte is dissolved in the same ACN-water mixture. The following steps are the same as in the protein case but taken in account the general changes mentioned in Chapter 6.

[4]A single crystal silicon substrate was used in the first experiment (Chapter 4) as a sample holder; later on ones made out of stainless steel.

[5]Scanning electron microscope

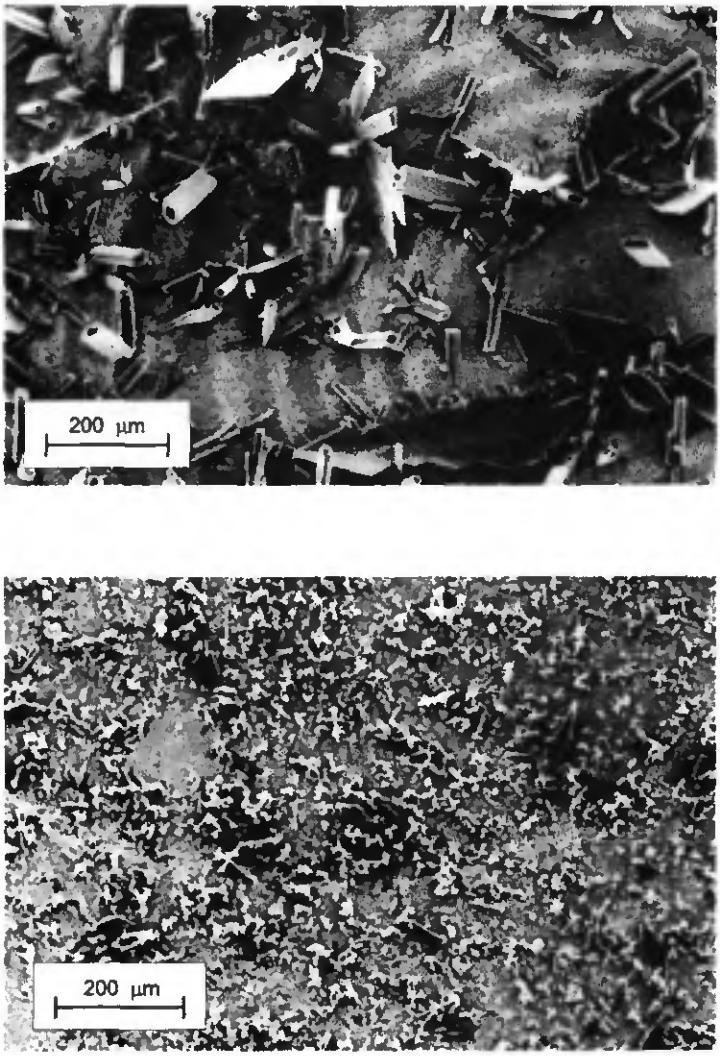

Figure 3.1: SEM pictures of sinapinic acid MALDI-probes. Top: A typical sample which has not been stirred while crystallization took place; this is not an useful probe. Bottom: A good sample – the crystal size is kept small by stirring.

3.2 Experimental setup

The basic experimental setup used in all experiments is illustrated in Figure 3.2 and described below. Differences from this main setup are mentioned in the corresponding chapters.

A pulse generator triggers externally the UV-laser[6] and the data-acquisition. The laser pulse is focussed onto the MALDI-probe to a spot size of $100 \times 100 \mu m^2$ using a UV-lens and mirrors. Since the reflected UV-laser light is also detected by superconducting tunnel junctions, no PIN-diode that would give the start signal for the TOF measurement was needed.

The MALDI-probe is connected electrically to an electrode held at high-voltage – typically 20 kV – delivered by a *Glassman* high-voltage supply. The entire surface of the MALDI-probe could be spotted by the laser thanks to a 2-axis UV-mirror. The mass spectrometer was evacuated by an *Alcatel* turbomolecular pump reaching a base pressure of 10^{-5} mbar in the chamber.

The mass spectrometer is coupled to a ^{3}He-cryostat provided by the Paul Scherrer Institut [97]. The base temperature of the cryostat measured with a calibrated Ge-thermistor from *LakeShore* is 450 mK, but the detectors themselves are at 0.6 K due to the infrared radiation. Three radiation shields had to be added to fight the thermal radiation; small holes in them assure that the macromolecules can reach the detectors. The junctions are mounted on a copper cold finger equipped with a fourth radiation shield. A ^{55}Fe-source[7] is fixed on this radiation shield resulting in a X-ray count rate of 0.3 Hz, low enough not to disturb the TOF measurements but providing the adjustment of the whole apparatus. Furthermore, the 6 keV pulses are used to calibrate the pulses due to macromolecule impacts.

An external Helmholtz coil ($B_{max} \approx 150$ Gauss) is used to suppress the Josephson supercurrent.

The charge sensitive preamplifiers based on the Amtek A250 preamp-chip (see Fig.3.3) are mounted inside the cryostat on a ≈ 170 K place. We installed three of them allowing us to evaporate three junctions on the same substrate and investigate pulse correlations between the junctions. Each junction can be individually current biased.

[6] A nitrogen laser from LSI, model VSL-337: wavelength 337 nm, pulse duration 3 ns, 100 μJ per pulse.

[7] A commonly used X-ray source. The two main lines: Mn K_α = 5.89 keV (89%) and Mn K_β = 6.49 keV (11%).

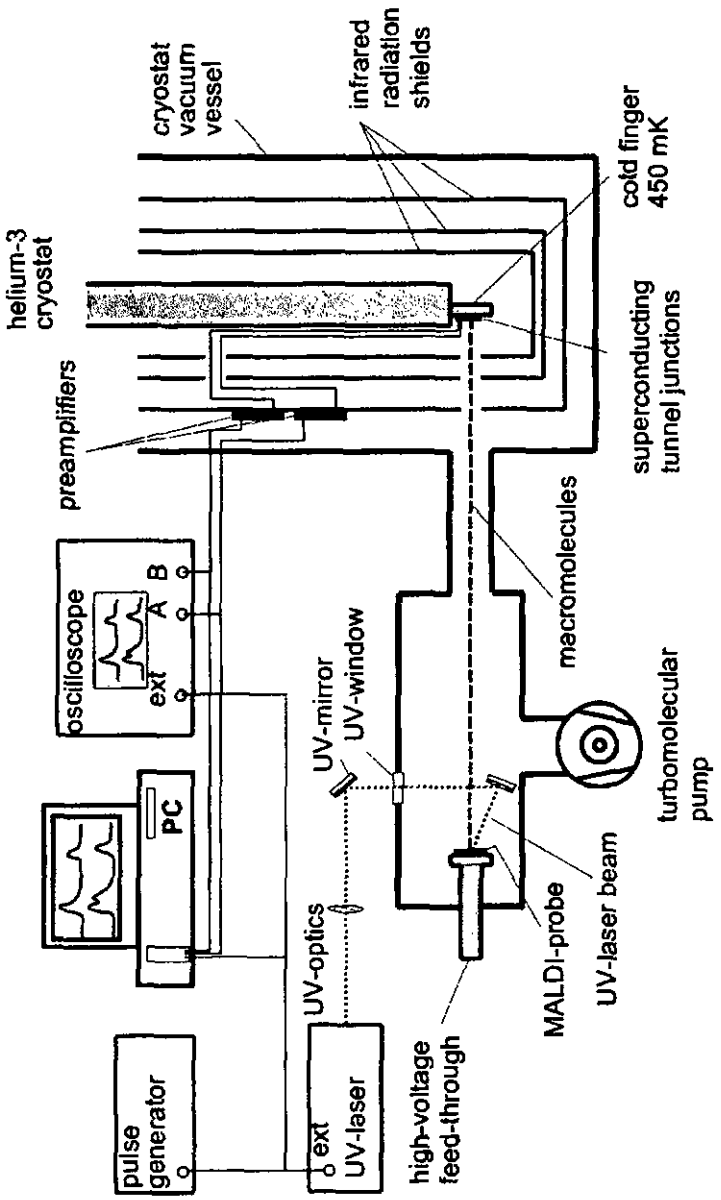

Figure 3.2: Experimental setup.

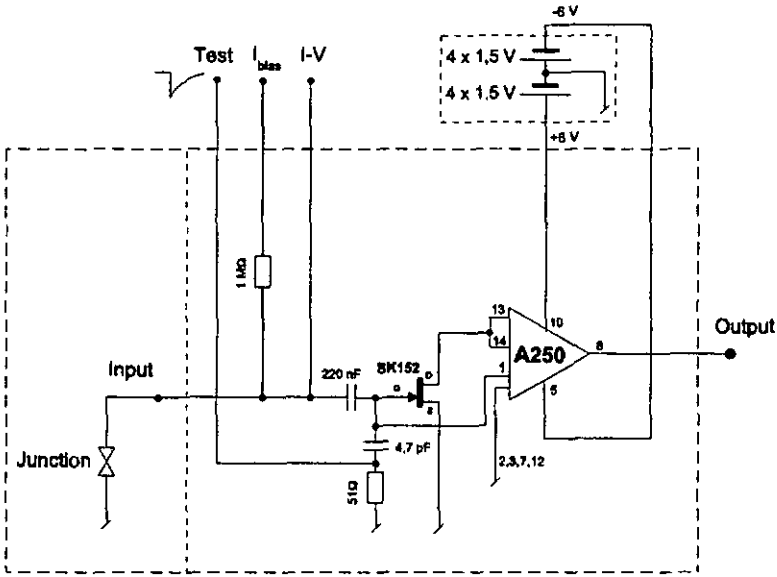

Figure 3.3: Scheme of the charge sensitive preamplifier based on the Amtek A250 preamplifier chip (Amtek Inc.) and a J-FET (SK152, Sony). The A250-internal feedback loop consists of an integrating capacitance of 1 pF and a resistance of 300 MΩ. The passive elements are metal film resistors and plastic capacitors in order to run the preamplifier at ≈ 170K.

3.3 Cryogenic detectors

Three types of cryogenic particle detectors have been used during this work: shadow-mask tin SIS junctions, a hot-electron microcalorimeter and photolithographic tin SIS junctions.
The hot-electron microcalorimeter was fabricated by the NIST-Boulder group, the two other kinds were made in Neuchâtel.

We have chosen to start with (Sn/Sn-ox/Sn) junctions because they are easily fabricated and are proven to work fine: an energy resolution of 65 eV for 6 keV X-rays could be achieved with such devices under optimal conditions [98, 99]. Nevertheless, we will have to build in the near future other cryogenic detectors since tin tunnel junctions are hardly thermaly recyclable. For this purpose, the construction of an UHV evaporation chamber is under way.

3.3.1 Shadow-mask tin SIS tunnel junctions

These tin junctions were fabricated in a vacuum chamber (base pressure $2 \cdot 10^{-6}$ mbar) by thermally evaporating tin (99.999% pure tin granules from *Balzers*) from a tungsten boat. The geometry of the junctions is defined by mechanical masks (see Fig. 3.4). The thicknesses of the evaporated films are measured by a *Balzers* quartz-crystal thickness monitor calibrated with some (mechanical) alpha-step measurements. For all indicated thicknesses the tooling factor has been taken into account.

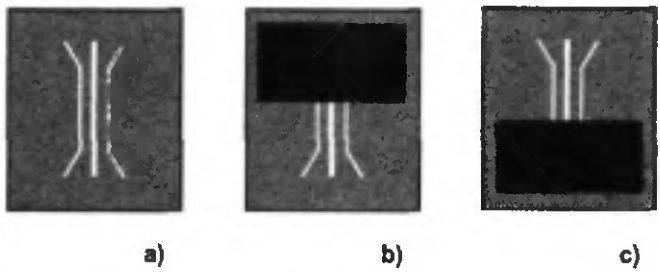

Figure 3.4: The shadow-mask technique. The mask a) defines the geometry of the junction. The first tin film is evaporated with the moving mask positioned as shown in b). After the oxidation the moving mask is shifted to the position showed in c). On the place of the small area which is always left free by the masks one will be having an overlap of both films: the sensitive area of the junction.

After having thoroughly cleaned the substrate, the first film was promptly deposited onto it. In order to increase the lifetime of the junctions, the evaporation of tin is performed in a slightly oxygenized atmosphere ($2 \cdot 10^{-5}$ mbar), making the tin films granular. The native oxide barrier is then built by oxidizing the first tin film by the DC glow discharge method [90] ($7 \cdot 10^{-2}$ mbar of O_2, voltage $\approx$ -800 V, oxidation time is a few minutes). After having moved the mask, the second tin film is again evaporated in the same low oxygen atmosphere. The deposition rate has initially to be kept very low to prevent the cracking of the thin oxide barrier. Both films have a thickness of 100 nm. The following figure shows the chosen geometry for these junctions.

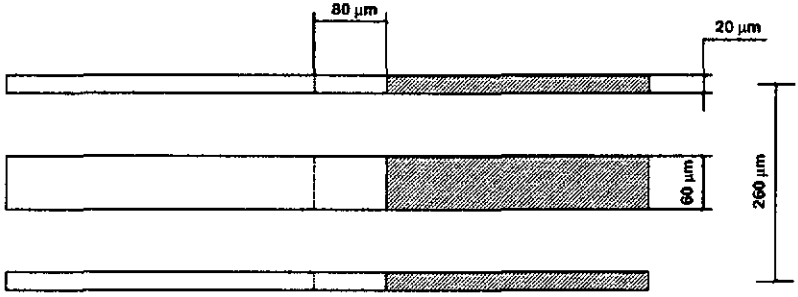

Figure 3.5: Geometry of our shadow-mask SIS tunnel junctions. The two outer junctions are identical while the middle one is four times larger. The sensitive area (overlap region) is $20 \times 80\mu m^2$ in the first case and $60 \times 80\mu m^2$ in the second.

The superconducting contact stripes are as large as the sensitive area causing nonnegligible quasiparticle diffusion.

3.3.2 Hot-electron microcalorimeter

This detector was made by the group headed by J. Martinis at the National Institute of Standards and Technology, Boulder CO, USA. They acquired, over the years, expertise with hot-electron microcalorimeters [92, 94].

In the used form it is a (Ag-absorber/Al_2O_3/Al) NIS junction, where the silver electrode absorbs the energy of the incoming particle and the tunnel junction measures the resulting electron temperature rise. The microcalorimeter is read out by an amplifier based on a series array low-noise high-bandwidth SQUID[8] [100]. A schematic of the detector, which is similar to the one described in [93], is illustrated in Figure 3.6 (see also Fig. 2.14, page 40).

The X-ray energy resolution at 6 keV is 92 eV full width at half maximum (FWHM).

[8]Superconducting quantum interference device

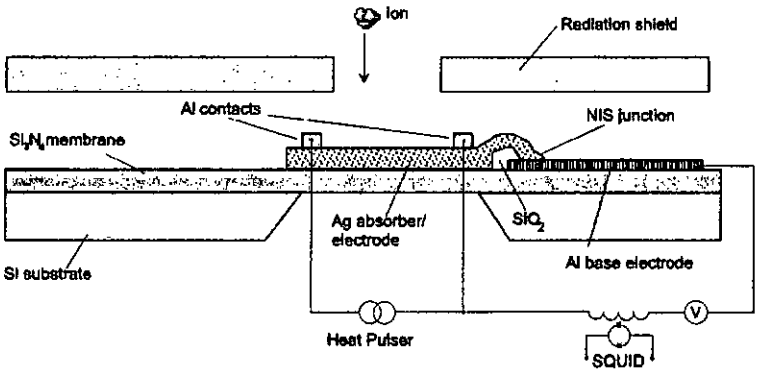

Figure 3.6: Scheme of the NIST hot-electron microcalorimeter. The absorbing metal electrode is made of silver (100nm thick; $200 \times 200\mu m^2$) deposited on a $0.5\mu m$ thin Si_3N_4 membrane. The NIS tunnel junction is formed by the overlap of the Ag electrode and the oxidized Al electrode. The aperture of the infrared radiation shield hold at 100 mK has a diameter of $200\mu m$. The heat pulser is used to simulate events.

The absorber is evaporated on a thin dielectric membrane to reduce phonon losses to the substrate. The electrons will relax with a time constant $\tau = C_e/G$, where C_e is the electronic heat capacity and G the total thermal conductance. Since G should be essentially the thermal conductance of the NIS junction, care has to be taken not to increase the thermal conductance while contacting the junction. This is avoided by using superconducting leads with critical temperatures T_c much higher than the working temperature: the thermal excitations are reflected at the interface to the superconductor ('Andreev reflection' [101]).

No Helmholtz coil is necessary since there is no Josephson supercurrent flowing in NIS junctions.

3.3.3 Photolithographic tin SIS tunnel junctions

The main advantage of using photolithographic techniques compared to the conventional shadow-mask technique lies in the fact that much finer geometric structures can be achieved. While fabricating very thin superconductive contact stripes of the junction one diminishes quasiparticle losses through them and hence increases the energy resolution of the detector.

In order to be as flexible as possible we chose to use only photonegative masks which are easily and quickly home-fabricated at low cost [102]. Based on the work of de Coulon [103] we were able to produce photoresist structures with an undercut as sketched in Figure 3.7 and photographed in Figure 3.8. By evaporating the tin[9] under an angle we got SIS junctions as shown in the Figures 3.9 to 3.11. The fabrication procedure is described in full detail in the diploma work of Grosjean [104].

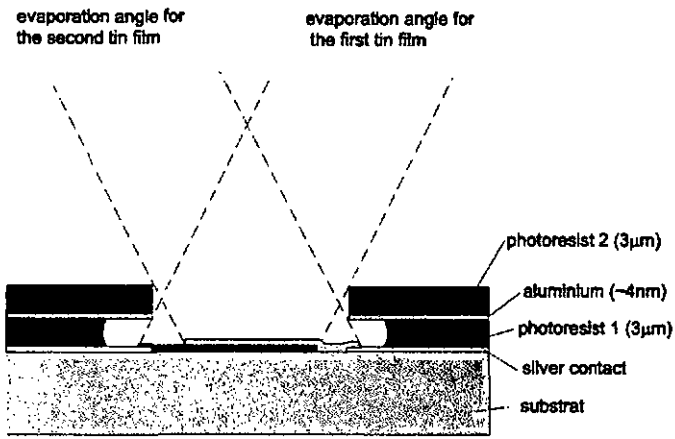

Figure 3.7: Sketch of the photoresist structure with an undercut permitting the evaporation of tin under an angle.

[9]The evaporation and the oxidation of the tin is made under the same conditions as in the shadow-mask case.

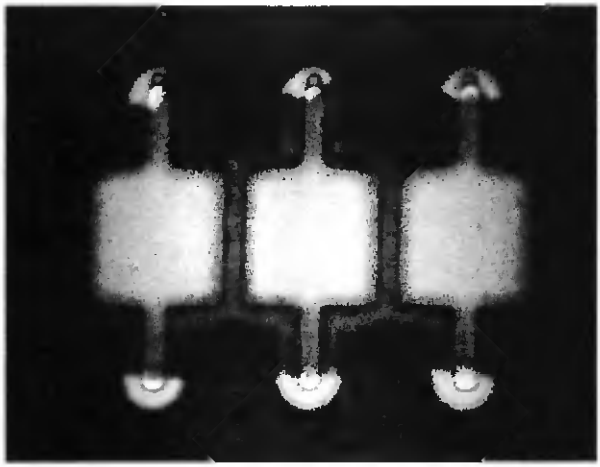

Figure 3.8: Photograph of a photoresist mask with a clearly visible undercut.

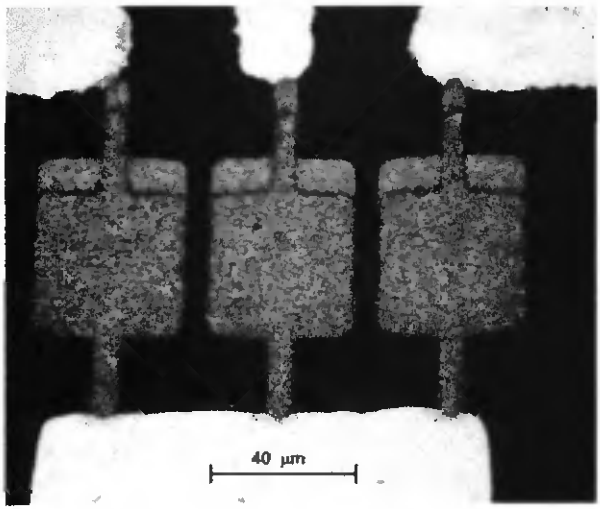

Figure 3.9: Photograph of a photolithographic tin junction.

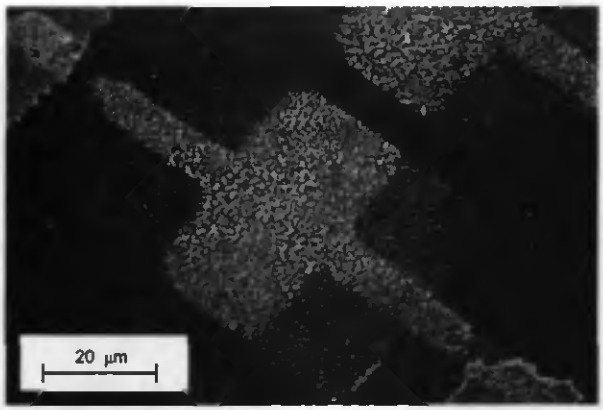

Figure 3.10: A SEM picture of one of our first photolithographic junctions. The sensitive area of this junction is rather small because we faced contact problems at that time forcing us to evaporate under wide angles. This problem is now solved as shown in Fig. 3.9.

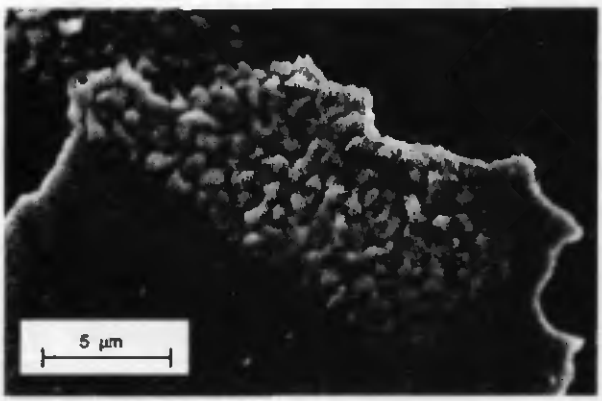

Figure 3.11: A detail of the junction recorded with a SEM, showing the pronounced granularity of the tin films.

To test if so fabricated STJs do function, we mount them in a single-shot ^{3}He-cryostat which is advantageous in reaching the base temperature (300 mK) in a short time. A ^{55}Fe X-ray source is placed 1 cm in front of the junctions. The pulses are amplified with an external preamplifier (the same as the one displayed at page 48). A typical pulse of a 6 keV X-ray, recorded with a digital memory oscilloscope after the preamplifier is depicted in Figure 3.12. If the junctions "do see" the 6 keV X-rays, we mount them in the big, coutinuous-cycle ^{3}He-cryostat to record a ^{55}Fe energy spectrum and then start the MALDI-TOF measurements. Figure 3.13 shows an energy spectrum of the ^{55}Fe source.

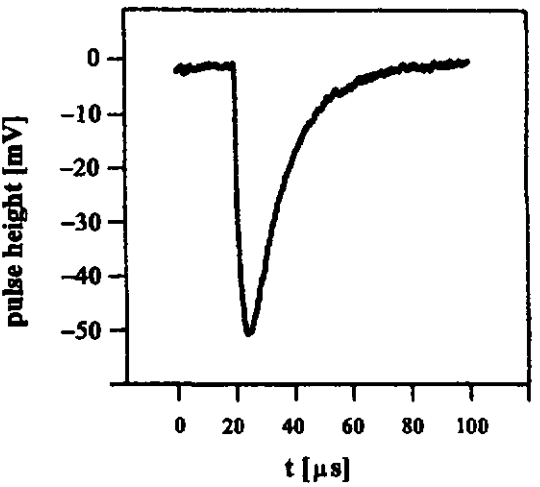

Figure 3.12: A typical 6 keV X-ray pulse after preamplification. The risetime is 2.3 μs and the fall time 30 μs.

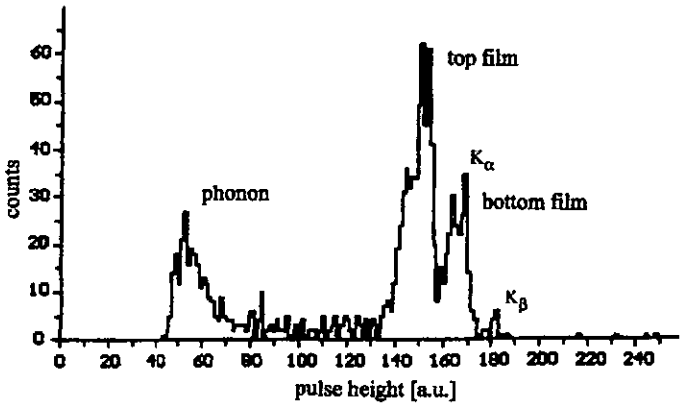

Figure 3.13: Energy spectrum obtained at 0.6 K from ^{55}Fe X-rays. At the low energy end we have the phonon peak caused by X-ray impacts near the junction and at higher energies the peaks caused by X-rays having interacted in the top, respectively in the bottom film. The two lines of the ^{55}Fe source are resolved: $K_\alpha = 5.89$ keV (89 %) and $K_\beta = 6.49$ keV (11 %). The energy resolution is $\Delta E \approx 150$ eV (FWHM).

Chapter 4

The first cryogenic detector mass spectrometry experiment

The first experiment ever done to detect macromolecules with a cryogenic particle detector has been performed at the Physics Institute of Neuchâtel by the Neuchâtel/GMU/PSI collaboration. B. van den Brandt from the Paul Scherrer Institute (PSI; Villigen, Switzerland) provided the continuous-cycle ^{3}He-cryostat mentioned in Section 3.2 and P.M. Gillevet from the George Mason University (GMU; Fairfax, Virginia, USA) was the biologist partner. It was a feasibility experiment: the aim was to find out as quickly as possible if yes or no it is possible to detect macromolecules with a cryogenic particle detector.
The results were published in 1996 in Applied Physics Letters [2].

4.1 Setup and samples

The experimental setup was as those described in Chapter 3. Exclusively the protein lysozyme (14'300 Da) was used; its MALDI-probe was prepared according to our standard recipe quoted in Section 3.1. As cryogenic detectors, the two thin shadow-mask tin SIS junctions (see Figure 3.5) have been used. The distance between the ion-source and the detectors was 105 cm.

4.2 Results

Figure 4.1 shows a typical single-shot event recorded with a digital memory oscilloscope showing the simultaneous response of the two junctions. The acceleration voltage was 10 kV. The first pulse (from the left) is caused by

the reflected laser pulse. The energy of a single UV-photon is 3.7 eV[1], high enough to break Cooper pairs; many of them hit the junctions at the same time. The slope of this reflected laser pulse defined the starting point of the time-of-flight measurement. A few μs later the pulses due to the (light) matrix molecules arrived. Finally, the pulses caused by macromolecule impacts occurred – the higher the mass-to-charge ratio m/q, the later the arrival.

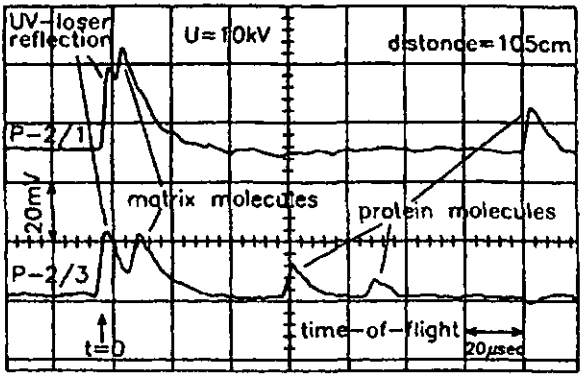

Figure 4.1: A typical time-trace showing the simultaneous response of the two junctions to one laser desorption event. The ions were accelerated by a potential difference of 10 kV.

As one can see in Figure 4.1, the risetime of these pulses was rather long. Although this fact is not a hindrance for a test experiment, significant faster detectors are required for serious mass spectrometry applications; fortunately they exist [77, 78, 84].

Since we had some margins in the signal-to-noise ratio, we could make our detectors faster by pulse-shaping the signals (τ = 500 ns) resulting in a time precision of a few 100 ns.

The electronic circuit for the time-of-flight measurements was, for each junction, as follows: the output of the preamplifier was connected via an Ortec 454 Timing Filter Amplifier to the input of a Cslite ADC card[2] plugged into a PC clone running a home-made data analysis program.

[1] $E = \hbar\omega = 2\pi\frac{\hbar c}{\lambda}|_{\lambda=337nm} = 3.7\,eV$

[2] An 8-bit analog-to-digital converter card with a choice of 2, 5 or 10 MHz sampling rate. 5 MHz has been used.

The 50 μs preceding the TTL laser trigger and the following 200 μs of each event was digitized and stored in the PC. Time-of-flight spectra were obtained by measuring offline the time differences between the reflected laser pulse and the following pulses due to molecule impacts.

Figure 4.2 shows a time-of-flight spectrum acquired at 20 kV acceleration voltage. There are clearly visible peaks corresponding to the sinapinic acid molecules ($t_{tof} = 8$ μs) and the single lysozyme protein ($t_{tof} = 63$ μs). Peaks due to dimers and higher mass multiplicities up to an indication for the $4m^+$ case have also been recorded. So we can state that we were able to detect macromolecules with masses up to $\approx$50 kDa.

From the Equation 1.6 we get

$$\frac{\Delta m}{m} = 2 \cdot \frac{\Delta t_{tof}}{t_{tof}} \ , \tag{4.1}$$

thus the single time-bin peak (time-bin = 350 ns) of the main lysozyme peak corresponds to a Δm of 100 Da (FWHM) giving a mass resolution $\frac{m}{\Delta m} = 143$.

All the pulses due to macromolecule impacts had approximately the same pulse height indicating that all molecules have deposited the same energy regardless their mass. We compared these pulses with the 6 keV X-ray pulses and concluded that a substantial part of the kinetic energy is absorbed by the junctions.

Furthermore, the sensitive area of each junction ($20 \times 80 \mu m^2$) is very small compared to the calculated section of the molecular beam (ø 5mm). Mostly a few molecules are expected to hit a detector per laser desorption. This statistical argument emphasizes that we have been detecting impacts of *single* macromolecules and *not* multiple hits.

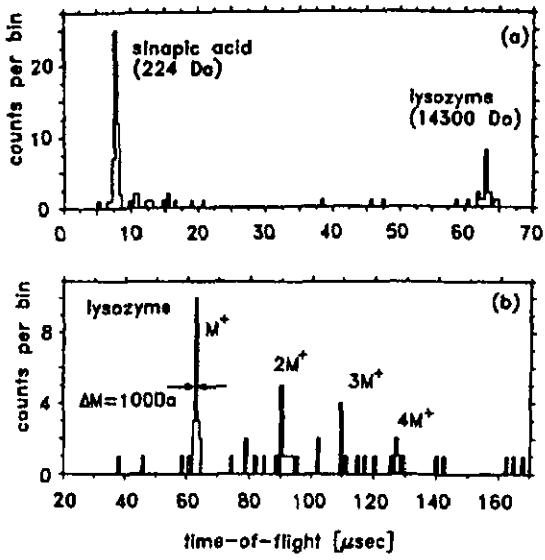

Figure 4.2: A lysozyme time-of-flight spectrum, acquired at 20 kV acceleration voltage. a): the time portion 0 - 70μs (time-bin = 350 ns) shows clearly the sinapinic acid matrix peak and the (singly) charged main peak of lysozyme. h) also reveals the higher mass multiplicities of lysozyme (time-bin = 850 ns).

4.3 Conclusions

The results were obtained by simple shadow-mask Sn/Sn-ox/Sn tunnel junctions.

With this first experiment we could prove the possibility of detection of macromolecules with cryogenic particle detectors. Single impacts of the protein lysozyme (molecular weight = 14300 Da) have been recorded. Also higher mass multiplicities were seen, with masses up to 50 kDa. By comparing the pulse heights of 6 keV X-rays and lysozyme ions with a kinetic energy of 20 keV we concluded that a substantial part of the kinetic energy was deposited in the cryogenic detector. The mass resolution was $\frac{m}{\Delta m} = 143$.

Chapter 5

Measurements with the hot-electron microcalorimeter

These experiments were performed in winter 96/97 by the NIST/Neuchâtel/GMU collaboration at the National Institute of Standards and Technology in Boulder (NIST; Boulder, Colorado, USA). We contributed by fabricating a small MALDI-TOF mass spectrometer and sending it with all required by-products (UV-laser, high-voltage supply, ...) to the United States. P.M. Gillevet from the George Mason University (GMU; Fairfax, Virginia, USA) was again the biologist partner.

The results were published in 1998 in Nature [3] and have been presented at the LTD-7 conference [5].

5.1 Setup and samples

As cryogenic particle detector the hot electron microcalorimeter described in Section 3.3.2 was used; it was mounted on an adiabatic demagnetisation refrigerator (ADR) reaching the necessary 100 mK working temperature. This cryogenic set was provided and run by the NIST-group.

The experimental setup differed slightly from the one described in Section 3.2 as shown in Fig. 5.1.

Mainly the two proteins lysozyme (14'300 Da) and bovine serum albumin (BSA, 66'430 Da) have been used. The MALDI-probes have been prepared according to our standard recipe quoted in Section 3.1 with the difference that no infrared lamp was used to accelerate the drying of the samples.

The output of the SQUID preamplifier was wired to a 20 MHz 12-bit analog-to-digital converter. A 4096-samples time trace has been recorded for

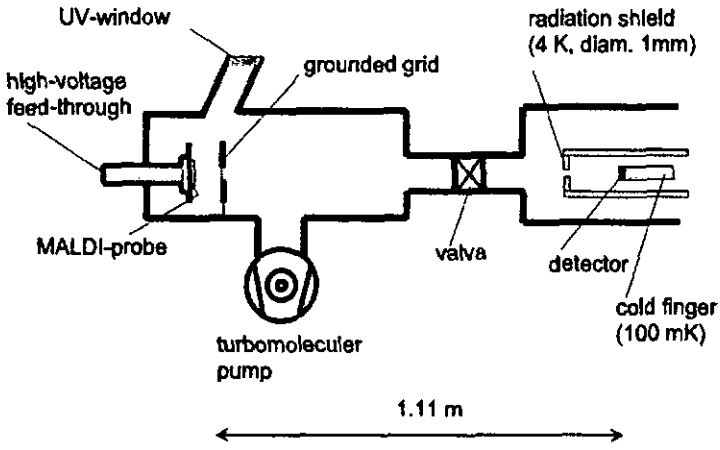

Figure 5.1: Experimental setup for the time-of-flight measurements at NIST. The 110 l/s turbomolecular pump reached a base pressure of $2 \cdot 10^{-7}$ mbar in the flight tube. A fine-mesh grid at ground potential has been added. One infrared radiation shield is fixed at 4 K, another one (pinhole $\phi 200 \mu$m) as indicated in Fig. 3.6 (p. 52) at 100 mK.

each laser desorption event; either at 10 MHz sampling rate (time-bin = 100 ns) or at full speed (time-bin = 50 ns).

5.2 Results

Figure 5.2 illustrates a time trace showing first (from the left) the reflected laser pulse (delayed by the turn-on time of the laser) and then two pulses caused by impacts of BSA proteins.

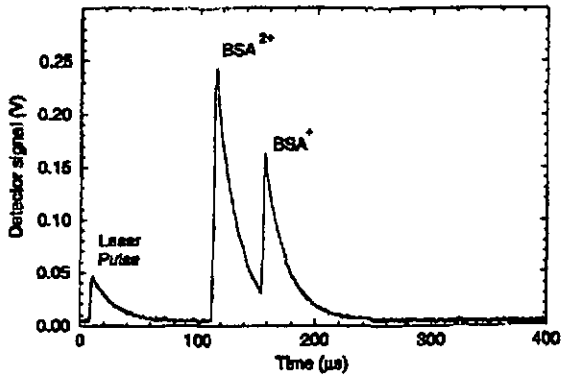

Figure 5.2: Time trace showing the response of the detector to one laser desorption event.

The signal risetime was 1.2 μs allowing an impact determination with a precision of roughly 200 ns. The slow relaxation of the detector (fall time 17 μs) could have caused pile-up problems which however could be managed thanks to the linearity of the detector, the 12-bit digitization and the low molecule impact rate.

From the fact that the stopping power is very high for macromolecules with a kinetic energy of a few tens keV – they interact at the surface of the detector – and from the imposing signal-to-noise ratio we conclude that the molecule detection efficiency is 100% for this detector.

The assignment of the pulses was made easier by the energy-resolving capability of the detector: Since the pulse height of the first molecule pulse in Fig. 5.2 is twice as high as the second one, the double kinetic energy was deposited, i.e. it must have been a doubly charged ion. Knowing the charge, the time-of-flight tells us that the first molecule pulse was caused by a doubly charged monomer (BSA^{2+}). With the same reasoning we matched the second molecule pulse to a singly charged monomer (BSA^{+}).

Doing this for hundreds of events one can get a scatter plot of deposited energy vs. time-of-flight. Figure 5.3 shows such a scatter plot obtained for the protein BSA in a sinapinic acid matrix, acquired at an acceleration voltage of 20 kV. Clearly visible the energy banding caused by the discrete

ionization states of the molecular ions and revealed by the energy resolving capability of the used cryogenic detector.

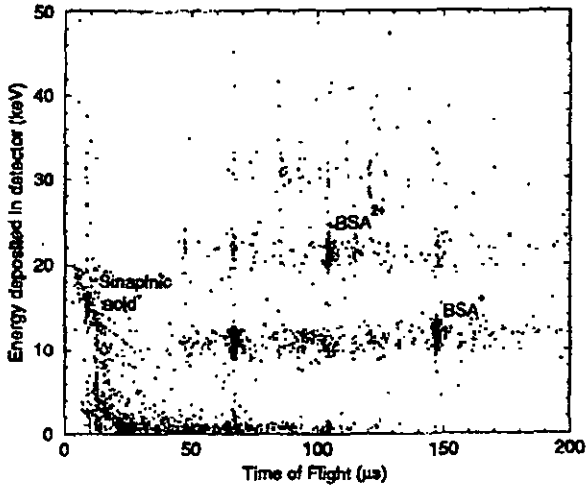

Figure 5.3: Scatter plot of deposited energy vs. time-of-flight of the BSA ion.

This scatter plot can also be transformed into a TOF histogram. Figure 5.4.a) shows the full histogram while in the histogram of Figure 5.4.b) only the events with an energy between 5 keV and 15 keV are included. This energy band corresponds to the selection of events of only singly charged ions. As one can see, the peak corresponding to the doubly charged monomer, as well as a lot of the background has been removed.

The peak at $t_{tof} = 67$ μs corresponds to an unidentified fragment with a mass m $\approx$ 14 kDa.

The time resolution of 1.3 μs (FWHM) for the BSA monomer peak implies a mass resolution $m/\Delta m = 56$. Similar results have been obtained for the same protein [45]: 90 for a SEM and 120 for a Faraday cup charge detector.

An intriguing fact visible in the Figure 5.3 is, that the molecular ions did not deposit all their kinetic energy in the detector. For example a BSA^+ ion accelerated by a 20 kV potential difference left only around 10 keV in

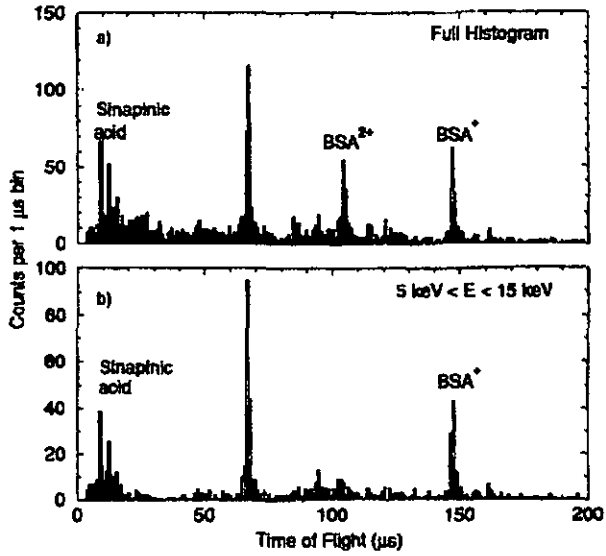

Figure 5.4: Time-of-flight histogram for the protein BSA, acquired at an 20 kV acceleration voltage. a) shows the full histogram; in b) only the points with a deposited energy between 5 keV and 15 keV are included, showing that the peak assigned to the douhly charged monomers disappeared.

the detector. The ratio of deposited energy in detector to kinetic energy was somewhat higher for the sinapinic acid ions: about 70%.

Figure 5.5 shows the ratio of deposited energy to kinetic energy vs. the kinetic energy for the three used molecules. It seems that this ratio does not depend on the kinetic energy with the exception of an indication of an increased ratio at lower energies. Furthermore, for molecules above a certain size, the ratio of deposited energy to kinetic energy seem to be $\approx$ 50% – this hypothesis is enforced by preliminary experiments with immunoglobulin G (IgG, 130 kDa) which were showing the same asymptotic limit. These observations imply that a molecular ion impact cannot he modeled as a rigid object hitting and sticking to the detector. The missing energy is prohably lost by ejected fragments upon impact.

The only previous experiment that measured the fractional energy deposition [58] has been performed with a niohium[1] SIS tunnel junction. They

[1]Niohium (Nb) has a rather high critical temperature T_c = 9.2 K, i.e. a high gap Δ.

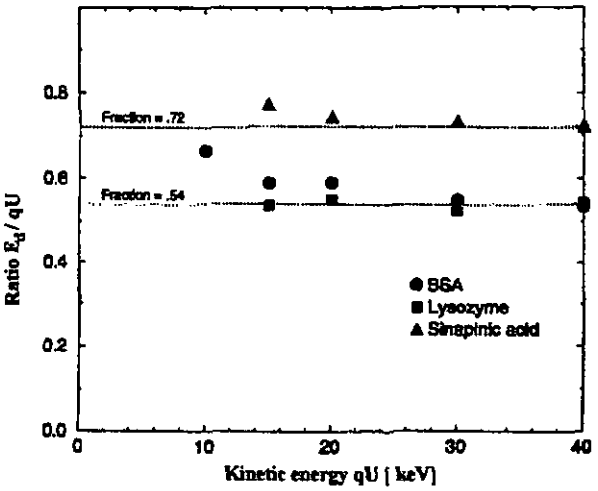

Figure 5.5: Ratio of deposited energy in the detector to kinetic energy vs. kinetic energy of the ion.

observed with a very similar protein (human serum albumin HSA, 66 kDa), accelerated by a potential difference of 25 kV, that only 20% of the kinetic energy is detected. This low percentage was explained by the fact that SIS tunnel junctions are not sensitive to subgap phonons (phonons with an energy smaller than the gap $2 \cdot \Delta$).

Later on we found with our improved tin junctions that 6 keV X-ray pulses are as high as macromolecule pulses of 6 keV kinetic energy (see Chapter 6). This discrepancy is not yet explained.

It is noteworthy that the energy resolution for the molecule impact events (20 kV) was 1.7 keV (FWHM) which is much worse than 92 eV (FWHM) for the 6 keV X-rays. This low energy resolution cannot be explained by the kinetic energy uncertainty implied by the time-of-flight uncertainty. This is an indication that the energy carried by the fragments flying apart upon impact is variable.

An experiment exploiting the energy-resolving capability of the detector has been performed to show the influence of the background pressure in the mass spectrometer. Lysozyme has a cross section for gas-phase scatter-

ing of about 15 nm^2. Thus the mean free path for lysozyme is 6 m in a nitrogen background pressure of $4 \cdot 10^{-7}$ mbar and 0.3 m in $8 \cdot 10^{-6}$ mbar. This explains the clear difference between the two scatter plots of Figure 5.6. The data from scatter plot a) were acquired when the pressure in the mass spectrometer was $4 \cdot 10^{-7}$ mbar and $8 \cdot 10^{-6}$ mbar in b). In both cases the acceleration voltage was 20 kV. In b) much more low energy noise signals are visible. This experiment illustrates the need of an excellent vacuum which has to prevail in the mass spectrometer if one wants to measure massive molecules. A similar quality degradation of mass spectra has been reported by Schuerch et al. [105] using glycol 4000 (mean molecular weight 4500 Da) in a pressure between $4 \cdot 10^{-6}$ mbar and $5 \cdot 10^{-7}$ mbar. Spengler et al. stated that the vacuum has to be better than 10^{-7} mbar for good quality high-mass TOF measurements [57].

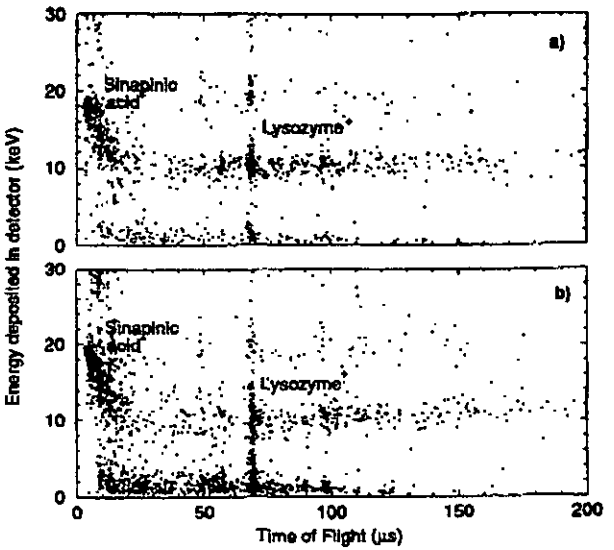

Figure 5.6: Influence of the background pressure in the mass spectrometer. The data in scatter plot of the deposited energy vs. time-of-flight were acquired in a pressure of a) $4 \cdot 10^{-7}$ mbar and b) $8 \cdot 10^{-6}$ mbar. Both cases were recorded with a potential difference of 20 kV.

5.3 Conclusions

Single macromolecule impacts of the proteins IgG (130 kDa), BSA (66 kDa) and lysozyme (14.3 kDa) have been recorded with a hot-electron microcalorimeter operated at 100 mK. Owing to the euergy-resolving capahility of the used cryogenic detector, a clear charge discrimination between singly and doubly charged ions could be made. It was found that macromolecules deposit only roughly 50% of their kinetic energy in the detector, independent of their kinetic energy (between 10 and 40 keV). The experiment stresses the need for a good vacuum in the mass spectrometer. The mass resolution for BSA was $m/\Delta m = 56$.

Chapter 6

Results with the photolithographic tin SIS junctions

In the end of '96 we commenced the fabrication of junctions using photolithographic techniques in order to get devices with an energy resolution high enough to be able to discriminate between singly and doubly charged ions. By March 97 we got the first devices and from May on we could use them in the mass spectrometer. These junctions are presented in section 3.3.3. The participants are the same as in the first experiment: Neuchâtel/GMU/PSI. The results have been presented at the LTD-7 conference [4] and an article is submitted for publication [6].

6.1 Setup and sample preparation

Several changes have been applied to the original setup (see chapter 3) to improve the mass spectrometer:

- A load-lock system has been added allowing a rapid sample change while maintaining a good vacuum in the spectrometer.
- A simple ion optic has been incorporated to increase the count rate and to perform delayed extraction. It is a double potential ion lens of the Wylie-McLaren type, see figure 6.1.
- We built two delayed extraction units; more about this extension is mentioned just below.
- A *Fug* high-voltage supply has been purchased whose polarity is quickly reversed and which has a digital voltage display yielding a more precise

determination of the acceleration voltage (+/- 100 V).

- Data are now stored on Iomega Zip drives.

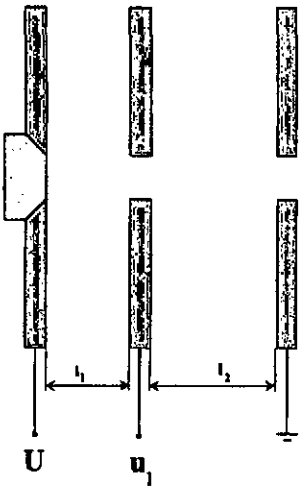

Figure 6.1: Sketch of our double potential ion optic. The potential U defines the kinetic energy of the ions and u_l the focal distance of the ion beam. The actual values for the electrode distances are l_1 = 0.5 inch and l_2=3/4 inch.

As already explained in the section 1.2.3, there are two reasons to use the delayed extraction: to increase the mass resolutioo and to allow the ions to be produced in a field free environment reducing fragmentation. Figure 6.2 shows the electronic scheme of our delayed extraction units (rise-time 40 ns). The measured turn-on delay time of our modules is 185 ns. Since the delay time of the laser is higher (460 ns), any delay time between -275 ns and a few seconds can be selected.

Concerning the **sample preparation** we reoounced to heat the sample solution with an infrared lamp since heating seems to give variable results [28]. We now speed up the drying by blowing softly dry nitrogen on the sample. Furthermore, we replaced the glass rod which was used to stir the sample by a plastic tip (a single-use plastic pipette where the tip has heen sealed by flaming it shortly).

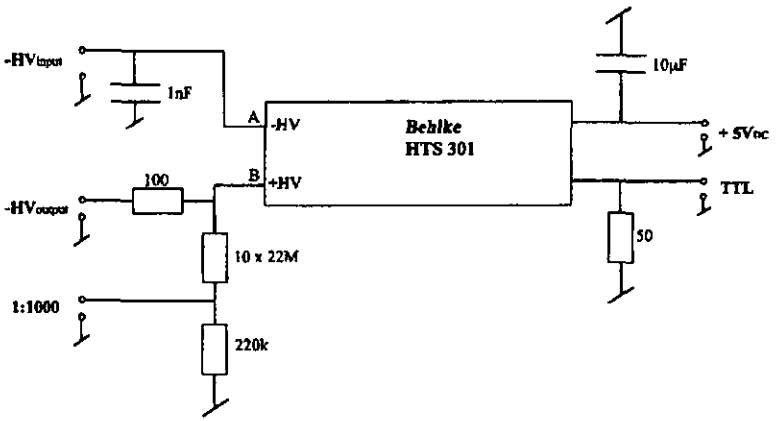

Figure fi.2: A delayed extraction unit is basically a fast high-voltage switch. We built two modules based on the fast high-voltage transistor switches of Behlke Electronic GmbH, Germany. One of the modules is for the acceleration electrode and the other unit for the second electrode of the ion lens (see fig. 6.1). We can switch up to 30 kV with these devices; the measured rise-time is about 40 ns. The showed configuration is for the 'negative pulse mode'; positive pulses are obtained by reversing A and B while applying a positive high-voltage to the entry. In our case we managed to select the polarity of the pulses by jumper-plugs. The 1:1000 output does not reflect the rise-time of the voltage at the electrodes, it is used to monitor the discharge of the high-voltage capacitor.

6.2 Results

1) Since we are working with three junctions at the same time, we can cross-check the results of each detector. Usually we record the simultaneous response of two junctions. Figure 6.3 shows time-of-flight spectra of the protein lysozyme (14'300 Da) acquired at 10 kV respectively 15 kV acceleration voltage. Clearly visible are the singly charged monomer peaks and the higher mass multiplicities up to the $5m^+$ case. As against the lysozyme spectrum of the first experiment (fig. 4.2, p. 62) the doubly charged monomer appeared now and more satisfactory: the count rate is good. Figure 6.4 presents a similar result of a IgG run (130 kDa) at 20 kV.

The mass resolution on the other hand is compromised by the use of

inappropriate amplifiers degrading the timing precision. Whilst improving continuously the quality of our detectors we faced problems to match the acquisition software and the postamplifiers to the bigger hence slower signals. The software could be steadily adapted to new situations but the hardware not, forcing us to use second-rate amplifiers unable to process the desired pulse shaping.

For the lysozyme main peak (15 kV) we got a timing resolution of 800 ns (FWHM) resulting in a mass resolution $m/\Delta m \simeq 50$ and for the 3 μs wide IgG main peak we found $M/\Delta M \simeq 35$.

We are confident to increase the mass resolution substantially in the near future with the new versatile postamplifiers which are under construction.

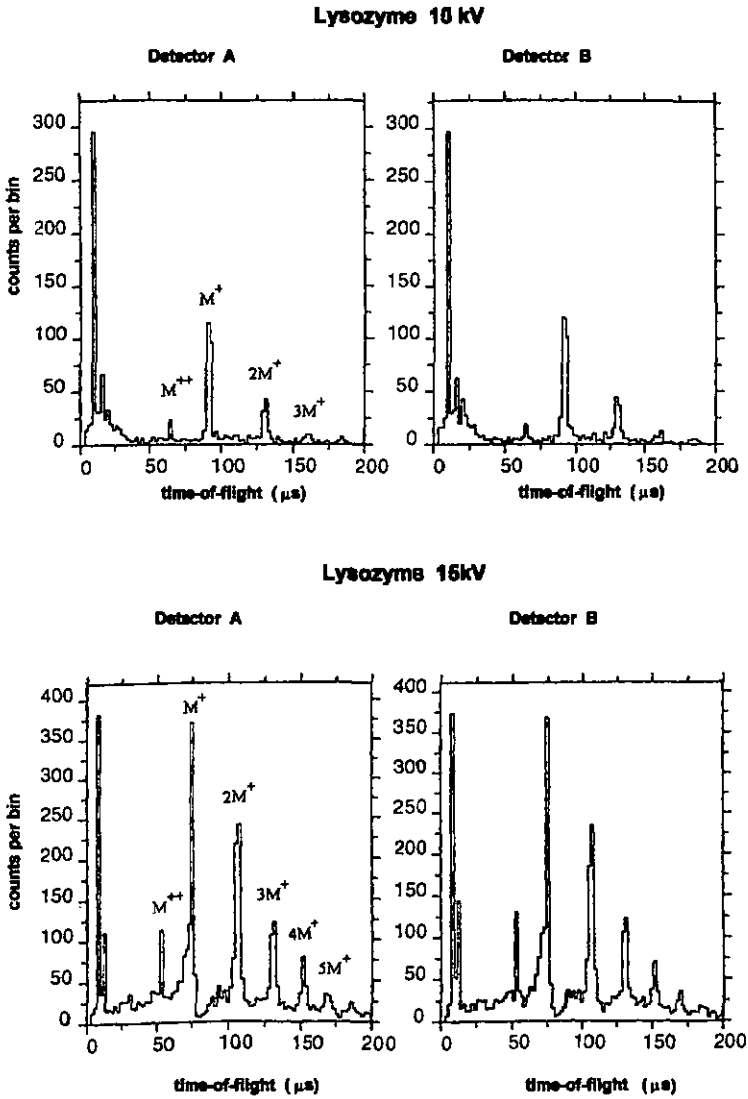

Figure 6.3: Time-of-flight spectra of lysozyme (14'300 Da) acquired at 10 kV respectively 15 kV acceleration voltage. The spectra of both detectors have been recorded simultaneously.

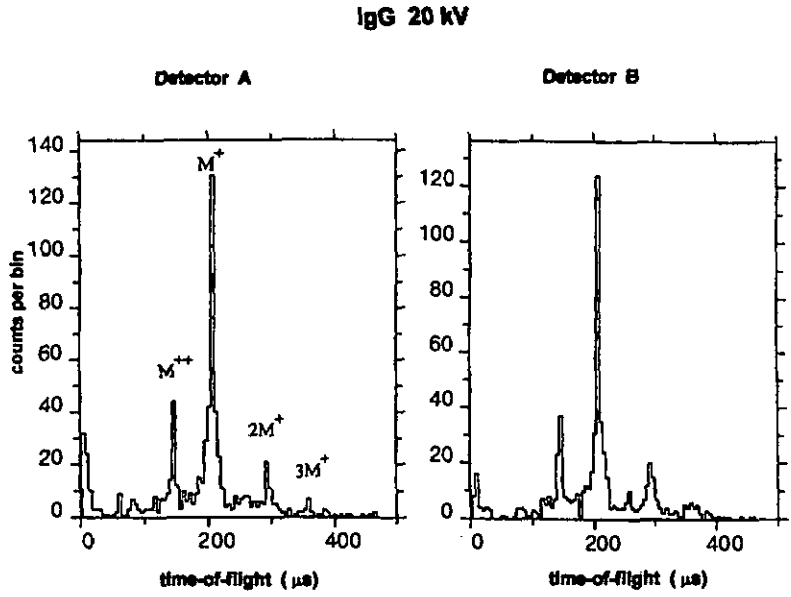

Figure 6.4: Time-of-flight spectra of the protein IgG (130 kDa) at 20 kV acceleration voltage.

2) The next figure is about charge separation. We recorded IgG spectra at 3 kV (2.8 kV), 6 kV (5.2 kV) respectively 12 kV (10.4 kV) acceleration voltage, see figure 6.5. The values in parentheses refer to the applied voltage to the second electrode of the ion optic. Several observations can be made on this experiment:

1. There is a clear **charge aeparation**. The doubly charged ions (M^{++}) have deposited more energy in the detectors than the singly charged ones (M^{+}). By applying an appropriate pulse height cut (i.e. energy cut) one can select the events with a definite charge state.

2. The comparison of the pulse heights of the IgG molecular ions with the pulse height of the 6 keV X-rays gives that the **macromolecules deposit 100 % of their kinetic energy**. We will elaborate this interesting point below.

3. The detectors are nonlinear above $\approx$ 12 keV.

4. **Time-of-flight consistency:** $t_{tof}(M^{++} @ 3\,kV) = t_{tof}(M^{+} @ 6\,kV)$ and $t_{tof}(M^{++} @ 6\,kV) = t_{tof}(M^{+} @ 12\,kV)$

5. **The sooner the impact, the smaller the relative pulse height;** i.e. the pulse height of a singly charged ion with a mass M will be somewhat smaller than the pulse height of a singly charged ion with a higher mass. Three explanations have been proposed for this behaviour, observed in all experiments performed with cryogenic detectors.

   (a) Higher mass ions can carry more internal energy and they get more kinetic energy in the desorption process.

   (b) The reflected laser pulse heats up the detector; the thermal relaxation time is – in our case – about 1 ms. Since the quasiparticle recombination rate increases strongly with the temperature at 0.6 K, the early siguals are smaller.

   (c) The LLNL/LBNL/Conductus collaboration proposed a model based on the ion fragmentation in the acceleration phase which could reproduce their scatter plots [61].

   The explanation given hy the LLNL/LBNL/Conductus collaboration may be correct for their scatter plots of comparatively poor quality but does not seem to be appropriate for ours. To find out to which extent the explanation (a) or (b) is correct, we have to do more research.

3) With the figure 6.6 we look a little hit closer at the 6 kV IgG scatter plot of fig. 6.5:
Figure 6.6 (a) shows again the 6 kV scatter plot of figure 6.5 and (b) is the corresponding time-of-flight spectrum which is somehow the vertical projection of (a). (d) shows the pulse height spectrum (horizontal projection of (a)) which has to be compared to the X-ray pulse height spectrum (c) recorded with identical parameters: Apparently the IgG ions with a kinetic energy of 6 keV leave the same energy (or even more) in the detector as 6 keV X-rays. This observation is in contradiction with the results obtained with Nb tunnel junctions [58, 59] and the hot-electron microcalorimeter (see chapter 5 and [3]), were the ion signals had only 20% respectively 50% of the corresponding X-ray pulse height. The explanation of this incidence is still not given; further experiments are planned to illuminate this point.

The pulse height spectrum (d) shows the 6 keV peak of the singly charged ions and the broader 12 keV peak of the doubly charged ones. Evidently the energy resolution is considerably worse for the ion impacts, a fact encountered in all experiments working with cryogenic detectors.

4) Furthermore we succeeded in detecting DNA-oligonucleotides: 40-mer, 70-mer and 120-mer in a 3-HPA matrix. 3-HPA has been proven to be a better matrix for DNA samples than the sinapinic acid [106]. These measurements have been performed with a delayed extraction time of 2 μs and at -12 kV acceleration voltage. Figure 6.7.a shows the time-of-flight spectrum of an equal molar concentration of the 40-mer (t_{tof} = 88 μs) and 70-mer (t_{tof} = 116 μs). The same peak heights indicate that the launch, ionization and detection efficiencies are the same for both oligomers. Figure 6.7.h shows a time-of-flight spectrum of 120-mer (t_{tof} = 152 μs) and fig. 6.7.c the result obtained for a plain 3-HPA matrix probe showing that the background of the oligomer spectra is largely due to matrix clusters.

6.3 Conclusions

The detectors used were tin SIS tunnel junctions operated at 0.6 K.
Single macromolecule impacts of the proteins lysozyme (14.4 kDa) and IgG (130 kDa) in a sinapinic acid matrix as well as DNA-oligonucleotides (40-mer, 70-mer and 120-mer) in a 3-HPA matrix have been detected. The charge state of the ions are determinable owing to the energy resolving capability of our detectors. The pulse height of a 6 keV ion impact is as high as a 6 keV X-ray pulse.

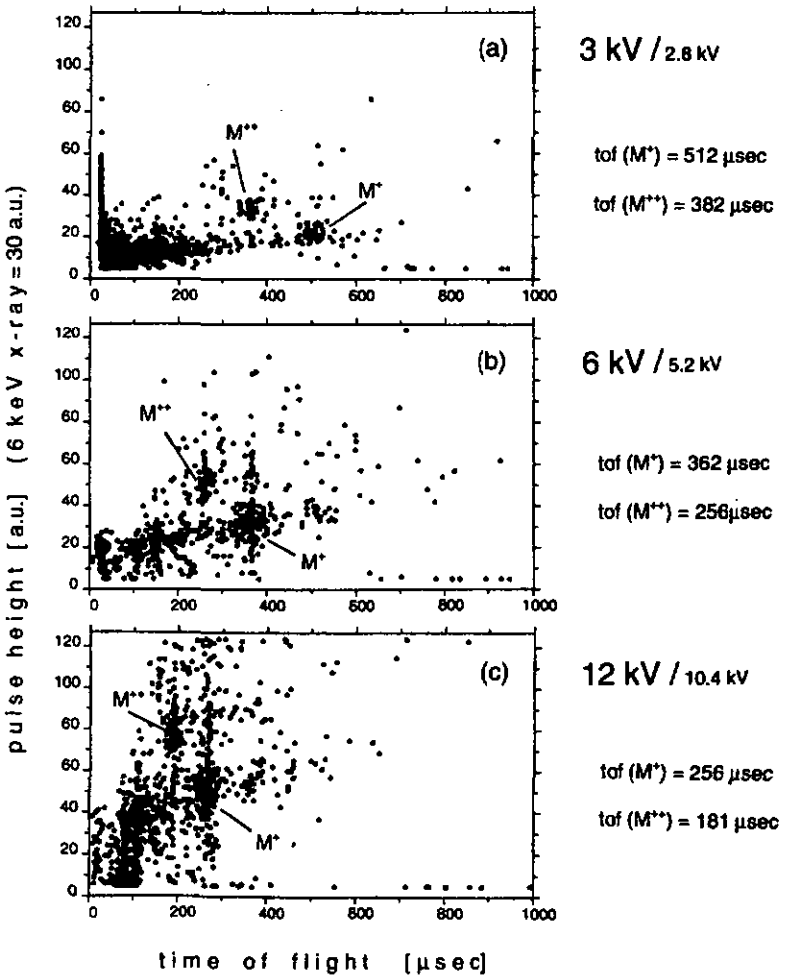

Figure 6.5: Time-of-flight and charge measurements of IgG (130 kDa) recorded at 3 kV (2.8 kV), 6 kV (5.2 kV) respectively 12 kV (10.4 kV) acceleration voltage. The values in parentheses refer to the applied voltage to the second electrode of the ion optic. A calibration with the ^{55}Fe source gives that the pulse height of 6 keV X-rays is 30 a.u..

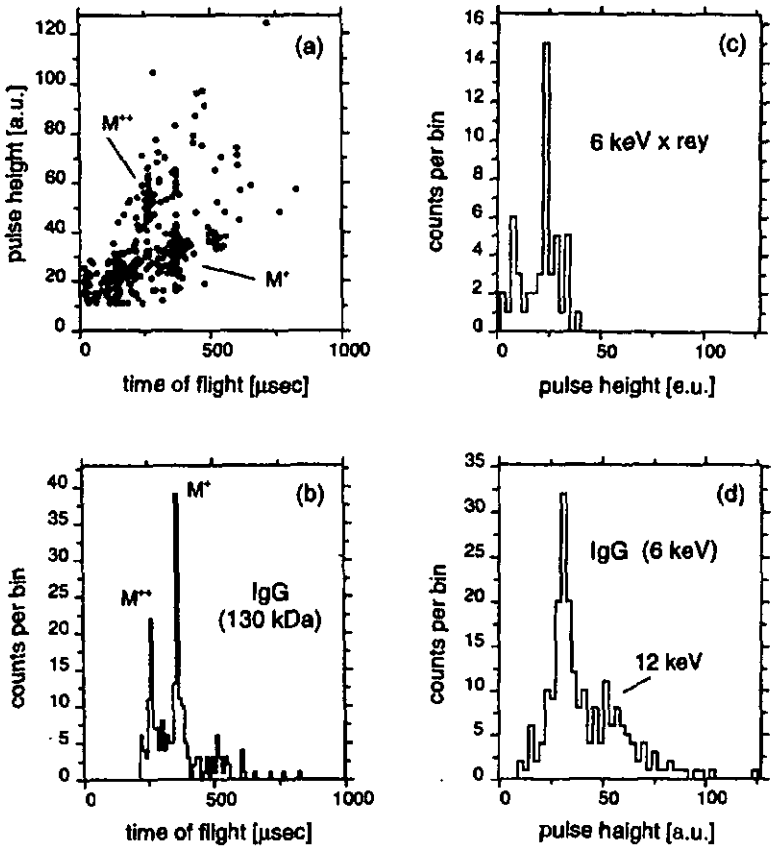

Figure 6.6: Time-of-flight and pulse height of IgG (130 kDa) at 6 kV acceleration voltage. Comparison of 6 keV pulse heights of ion impacts and X-ray hits.

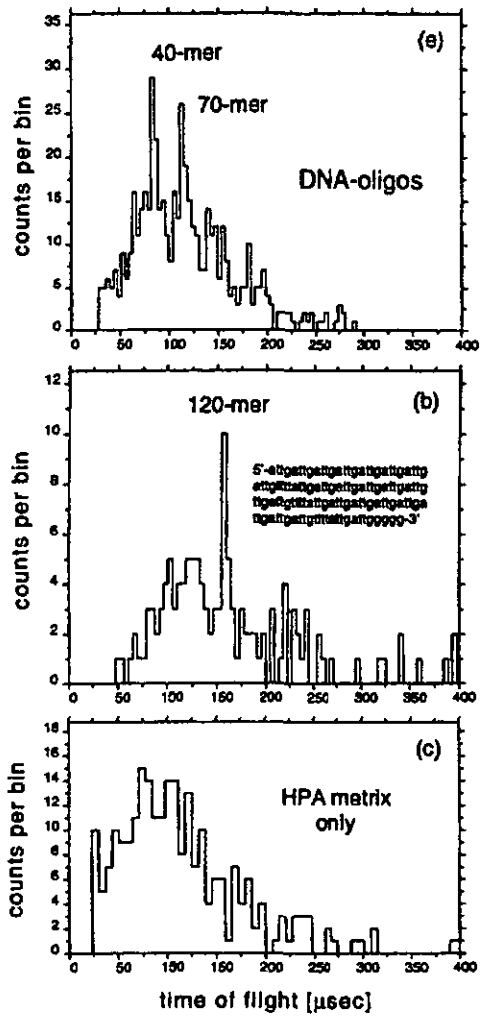

Figure 6.7: Time-of-flight spectra of DNA-oligomers in a 3-HPA matrix at -12 kV acceleration voltage.

Chapter 7

Conclusions

In this work it has been shown that cryogenic particle detectors can be used as ion detectors in the mass spectrometry of massive biopolymers. Owing to their calorimetrical detection scheme they have a *single* ion impact detection efficiency of 100%, independant of the ion mass and velocity.

From the large variety of existing low temperature detectors, the superconducting tunnel junction (STJ) and the hot-electron microcalorimeter has been picked-from to be investigated. The STJ was a Sn/Sn-ox/Sn tunnel junction operated at 0.6 K and the microcalorimeter (Ag-absorber/Al-ox/Al) was run at 100 mK.

Both detectors – although significantly different in their physical working principle – gave similar results with a MALDI TOF mass spectrometer:

- ***single* impacts of the proteins** lysozyme (14'300 Da), bovine serum albumin (66 kDa) and immunoglobulin G (130 kDa) have been recorded.
- these detectors are able to **determine the charge state** of the ion; by applying an appropriate pulse height cut one separates the singly from the doubly charged ions.

Furthermore, it has been shown that one should be having an excellent vacuum in the mass spectrometer in order to obtain good mass spectra.

In addition, we could detect **DNA-oligonucleotides** with a length of up to 120 bases. 40-mer, 70-mer and 120-mer gave comparable mass peaks indicating that the launch, ionization and detection efficiencies are the same. The mass resolution of our actual mass spectrometer is not high enough to resolve DNA-oligomers differing in length by one base (mass of one base $\approx$ 300 Da). We expect to improve significantly the mass resolution in the near future by

using better matched electronics, improving the quality of the vacuum in the flight path, exploiting fully the possibilities of delayed extraction and applying a more elaborate algorithm to determine the arrival of the ions (constant fraction triggering).

Two open questions remain:

1. How much of the ion kinetic energy is deposited in the detector? With the hot-electron microcalorimeter we found that the ratio of deposited energy in the detector to kinetic energy was 50% for macromolecules, while with the tin STJ the pulse height of a 6 keV X-ray is as high as an ion impact of the same energy. Another collaboration working with Nb STJs observed a ratio of only 20% [58]:

Detector		T_c [K]	Ratio E_d/qU	sensitive area [μm^2]
Nb STJ	@ 1.2 K	9.2	20%	200×200
Sn STJ	@ 0.6 K	3.7	100%	40×40
Ag absorber	@ 0.1 K	-	50%	200×200

2. It has been found that in Sn STJs the relative pulse height is higher for ions arriving later on the detector. We have to find out to which extent this is caused by the fact, that heavier molecules can carry more internal thermal energy (which is also detected by a cryogenic detector).

From our results we infer that cryogenic particle detectors are valid alternatives to the ion detectors based on the secondary electron multiplication and deserves therefore to be investigated further. We think that significant improvements can be achieved:

- As already mentioned, the timing resolution can be improved.
- The energy resolution, hence the charge separation capability, can be improved by using a shutter blocking off the reflected laser light and by adding a pinhole radiation shield directly mounted on the detector substrate.
- By using an UV-attenuator we can work near the threshold fluence yielding higher quality mass spectra.
- An UHV evaporation system is under construction, in order to build other cryogenic particle detectors to be examined.

Bibliography

[1] D. Twerenbold; *Biopolymer mass spectrometer with cryogenic particle detectors.* Pages 253-255 in [84].

[2] D. Twerenbold, J.-L. Vuilleumier, D. Gerber, A. Tadsen, B. van den Brandt and P.M. Gillevet; *Detection of single macromolecules using a cryogenic particle detector coupled to a biopolymer mass spectrometer.* Appl. Phys. Lett. **68**(24) (1996) 3503-3505.

[3] G.C. Hilton, J.M. Martinis, D.A. Wollmann, K.D. Irwing, L.L. Dulcie, D. Gerber, P.M. Gillevet and D. Twerenbold; *Impact energy measurement in time-of-flight mass spectrometry with cryogenic microcalorimeters.* Nature **391** (1998) 672-675.

[4] D. Gerber, C. Grosjean, D. Twerenbold, J.-L. Vuilleumier, P.M. Gillevet and B. van den Brandt; *Cryogenic particle detectors in biopolymer mass spectrometers.* Pages 73-75 in [85].

[5] G.C. Hilton, J.M. Martinis, D. Twerenbold, P.M. Gillevet, D.A. Wollman, K.D. Irwing, L.L. Dulcie and D. Gerber; *Microcalorimeter Particle Detector for Mass Spectrometry.* Talk given by G. Hilton at the seventh international Workshop on Low Temperatures Detectors in Munich (1997).

[6] D. Twerenbold, P.M. Gillevet, D. Gerber, G. Gervasio, J.-L. Vuilleumier and B. van den Brandt; *Single molecule detection of 120-mer DNA-oligonucleotides and 130 kDa IgG proteins with cryogenic particle detectors.* Submitted for publication (1997).

[7] M.W. Senko, F.W. McLafferty; *Mass Spectrometry of Macromolecules: Has Its Time Now Come?.* Annu. Rev. Biophys. Biomol. Struct. **23** (1994) 763-785.

[8] H. Ewald and H. Hintenberger; *Methoden und Anwendungen der Massenspektroskopie.* Chemie Verlag, Weinheim, 1952.

[9] M.S.B. Munson, H.F. Field; *Chemical Ionization Mass Spectrometry.* J. Am. Chem. Soc. **88** (1966) 2621-2630.

[10] J.A. Caroll and R.C. Beavis; *Matrix-Assisted Laser Desorption and Ionization*, Chapter 7 of *Laser Desorption and Ablation* in the series *Experimental Methods in the Physical Sciences*; Ed. J.C. Miller and R.F. Haglund, Jr. It can be downloaded from: http://128.122.10.3/MALDI/ChemPhysMan.htlm

[11] R.J. Beuhler, E. Flanigan, L.J. Green and L. Friedman; *Proton Transfer Mass Spectrometry of Peptides. A Rapid Heating Technique for Underivatized Peptides Containing Arginine.* J. Am. Chem. Soc. **96** (1974) 3990-3999.

[12] J.B. Fenn, M. Mann, C.K. Meng and C.M. Whitehouse; *Electrospray ionization – principles and practice.* Mass Spectrom. Rev. **9** (1990) 37-70.

[13] R.D. Smith, J.A. Loo, R.R. Ogorzalek, M. Busman and H.R. Udseth; *Principles and practice of electrospray ionization – mass spectrometry for large polypeptides and proteins.* Mass. Spectrom. Rev. **10** (1991) 359-451.

[14] A.P. Snyder ed.; *Biochemical and Biotechnological Applications of Electrospray Ionization Mass Spectrometry.* ACS Symposium Series **619**, American Chemical Society, 1996.

[15] A.P. Bruins, T.R. Covey, J.D. Henion; Anal.Chem. **59** (1987) 2642.

[16] P Arpino; *Combined liquid chromatography mass spectrometry. Part II. Techniques and mechanisms of thermospray.* Mass Spectrom. Rev. **9** (1990) 631-669.

[17] R. Feng, Y. Konishi; *Analysis of antibodies and other large glycoproteins in the mass range of 150'000-200'000 Da by electrospray ionization mass spectrometry. Anal. Chem.* **64** (1992) 2090-95.

[18] J.V. Iribarne, B.A. Thomson; J. Chem. Phys. **64** (1976) 2287.

[19] H.D. Beckey; *Field Ionization Mass Spectrometry.* Pergamon Press, Oxford, (1971).

[20] R.D. Macfarlane and D.F. Torgesson; *Californium-252 Plasma Desorption Mass Spectrometry.* Science **191** (1976) 920-925.

[21] G. Jonsson, A. Hedin, P. Håkansson, B.U.R. Sundquist, H. Bennich, P. Roepstorff; *Compensation for non-normal ejection of large molecular ions in plasma-desorption mass spectrometry.* Rapid. Commun. Mass Spectrom. **3** (1989) 190-191.

[22] A. Bennighoven and W.K. Sichtermann; *Detection, Identification and Structural Investigation of Biologically Important Compounds by Secondary Ion Mass Spectrometry.* Anal. Chem.**50** (1978) 1180-1184.

[23] M. Barber, R.S. Sedgwick and A.N. Tyler; *Fast Atom Bombardement of Solids (F.A.B.): A New Source for Mass Spectrometry.* J. Chem. Soc. Chem. Commun. (1981) 325-329.

[24] F. Hillenkamp; *Laser Induced Ion Formation from Organic Solids*, in *Ion Formation from Organic Solids*, pp.190-205, Ed. A. Bennighoven, vol. **25** Springer Series in Chemical Physics, Springer-Verlag, Berlin, 1983.

[25] K. Tanaka, H. Waki, Y. Ido, S. Akita, Y. Yoshida and T. Yoshida; *Protein and Polymer Analysis up to m/z 100,000 by Laser Ionization Time-of-Flight Mass Spectrometry.* Rapid Commun. Mass. Spectrom. **2** (1988) 151-153.

[26] M. Karas, D. Bachmann, U. Bahr and F. Hillenkamp; *Matrix-assisted ultraviolet laser desorption of non-volatile compounds.* Int. J. Mass Spectrom. Ion Proc., **78** (1987) 53-68.

[27] F. Hillenkamp, M. Karas, R.C. Beavis and B.T. Chait; *Matrix-assisted laser desorption/ionization mass spectrometry of biopolymers.* Anal. Chem. **63** (1991) A1193-203.

[28] R.C. Beavis and B.T. Chait; *Cinnamic Acid Derivatives as Matrices for Ultraviolet Laser Desorption Mass Spectrometry of Proteins.* Rapid Commun. Mass Spectrom. **3** (1989) 432-435.

[29] W. Ens, Y. Mao, F. Mayer and K.G. Standing; *Properties of Matrix-assisted Laser Desorption. Measurements with a Time-to-Digital Converter.* Rapid.Commun. Mass Spectrom. **5** (1991) 117-123.

[30] P. Demirev, A. Westman, C.T. Reimann, P. Håkansson, D. Barowsky, B.U.R. Sundquist, Y.D. Cheng, W. Seibt and K. Siegbahn; *Matrix-assisted Laser Desorption with Ultra-short Laser Pulses.* Rapid Commun. Mass Spectrom. **6** (1992) 187-191.

[31] A. Westman; *Matrix-Assisted Laser Desorption and Ionization of Biomolecules.* Acta Universitatis Upsaliensis, Uppsala, 1994.

[32] R.C. Beavis and B.T. Chait; *Matrix-assisted Laser-desorption Mass Spectrometry Using 355 nm Radiation.* Rapid Commun. Mass Spectrom. **3** (1989) 436-439.

[33] R.C. Beavis and B.T. Chait; *Velocity distributions of intact high mass polypeptide molecule ions produced by matrix assisted laser desorption.* Chem. Phys. Letters **181** (1991) 479-484.

[34] R.W. Nelson, D. Dogruel and P. Williams; *Detection of human IgM at $m/z \approx 1$ MDa.* Rapid Commun. Mass Spectrom. **9** (1995) 625.

[35] M. Karas, U. Bahr and U.Giessmann; *Matrix-assisted laser desorption ionization mass spectrometry.* Mass Spectrometry Reviews **10** (1991) 335-357.

[36] M.V. Buchanan and R.L. Hettich; *Fourier Transform Mass Spectrometry of High-Mass Biomolecules.* Anal. Chem. **65** (1993) A245-A259.

[37] W. Paul and H. Steinwedel; *Ein neues Massenspektrometer ohne Magnetfeld.* Z. Naturforschung **8a** (1953) 448-450.

[38] Balzers AG; *Partial pressure measurement in vacuum technology.* BG 800 169 PE(8703), Fürstentum Liechtenstein.

[39] M. Comisarow and A.G. Marshall; *Fourier Transform Ion Cyclotron Resonance Spectroscopy.* ASMS Conference R5 (1975) 453-454.

[40] R.J. Cotter ed.; *Time-of-Flight Mass Spectrometry.* ACS symposium series **549**, American Chemical Society, Washington DC, 1994.

[41] B.A. Mamyrin, V.I. Karataev, D.V. Shmikk and V.A. Zagulin; *The mass-reflectron, a new nonmagnetic time-of-flight mass spectrometer with high resolution.* Sov. Phys. JETP **37** (1973) 45-48.

[42] W.C. Wiley and I.H. McLaren; *Time-of-Flight Mass Spectrometer with Improved Resolution.* Rev. Sci. Instrum. **26** (1955) 1150-1157.

[43] M.T. Roskey et al.; *DNA sequencing by delayed extraction-matrix-assisted laser desorption/ionization time-of-flight mass spectrometry.* Proc. Nat. Acad. Sci. USA, **93** (1996) 4724-4729.

[44] D.C. Imrie, J.M. Pentney and J.S. Cottrell; *A Faraday Cup Detector for High-mass Ions in Matrix-assisted Laser Desorption/Ionization Time-of-flight Mass Spectrometry.* Rapid Commun. Mass Spectrom. **9** (1995) 1293-1296.

[45] U. Bahr, U. Röhling, C. Lautz, K. Strupat, M. Schürenberg and F. Hillenkamp; *A charge detector for time-of-flight mass analysis of high mass ions produced by matrix-assisted laser desorption/ionization (MALDI).* Int. J. Mass Spectrom. Ion Processes **151** (1996) 9-21.

[46] M.A. Park and J.H. Callahan; *An inductive Detector for Time-of-flight Mass Spectrometry.* Rapid Commun. Mass Spectrom. **8** (1994) 317-322.

[47] GALILEO Electro-Optics Corporation; *Channeltron© Electron Multiplier Handbook for Mass Spectrometry Applications*, 1991.

[48] J.L. Wiza; *Microchannel Plate Detectors.* Nucl. Instr. Meth. **162** (1979) 587-601.

[49] E.A. Kurz; *Channel electron multipliers.* American Laboratory, March 1979, p. 67.

[50] S. Dhawan; IEEE Trans. Nucl. Sci NS-**30**, (1981), 672.

[51] W.R. Leo, *Techniques for Nuclear and Particle Physics Experiments*, Springer Verlag, Berlin, Heidelberg, 1987.

[52] R.J. Beuhler and L. Friedman; *Threshold studies of secondary electron emission induced by macro-ion impact on solid surfaces.* Nucl. Instr. Meth. **170** (1980) 309-315.

[53] P.W. Geno and R.D. Macfarlane; *Secondary electron emission induced by impact of low-velocity molecular ions on a microchannel plate.* Int. J. Mass Spectrom. Ion Processes **92** (1989) 195-210.

[54] J. Martens, W. Ens, K.G. Standing and A. Verentchikov; *Secondary-ion and Electron Production from Surfaces Bombarded by Large Polyatomic Ions.* Rapid Commun. Mass Spectrom. **6** (1992) 147-157.

[55] D.F. Barofsky, G. Brinkmalm, P. Håkansson and B.U.R. Sundqvist; *Quantitative determination of kinetic energy releases from metastable decompositions of sputtered organic ions using a time-of-flight mass spectrometer with a single-stage ion mirror.* Int. J. Mass Spectrom. Ion Processes **131** (1994) 283-294.

[56] G. Westmacott, W. Ens and K.G. Standing; *Secondary ion and electron yield measurements for surfaces bombarded with large molecular ions.* Nucl. Instr. Meth. **B 108** (1996) 282-289.

[57] B. Spengler, D. Kirsch and R. Kaufmann; *Metastable Decay of Peptides and Proteins in Matrix-assisted Laser-desorption Mass Spectrometry.* Rapid Commun. Mass Spectrom. **5** (1991) 198-202.

[58] M. Frank, C.A. Mears, S.E. Labov, W.E. Benner, D. Horn, J.M. Jaklevic and A.T. Barfknecht; *High-efficiency Detection of 66'000 Da Protein Molecules Using a Cryogenic Detector in a Matrix-assisted Laser Desorption/Ionization Time-of-flight Mass Spectrometer.* Rapid Commun. Mass Spectrom. **10** (1996) 1946-1950.

[59] W.H. Benner, D.M. Horn, J.M. Jaklevic, M. Frank, C. Mears, S. Labov and A.T. Barfknecht; *Simultaneous Measurement of Flight Time and Energy of Large MALDI Ions with a Superconducting Tunnel Junction Detector.* To be published in J. Am. Soc. Mass Spectrom. (1997).

[60] S.E. Labov, M. Frank, J.B. le Grand, M.A. Lindemann, H. Netel, L.J. Hiller, D. Chow, S. Friedrich, C.A. Mears, G. Caldara and A.T. Barfknecht; *Cryogenic detector developement at LLNL: ultraviolet, X-ray, gamma-ray and biomolecule spectroscopy.* Pages 82-95 in [85].

[61] M. Frank; *High-mass biomolecule Mass Spectrometry with Cryogenic Detectors.* Talk given at the seventh international Workshop on Low Temperature Detectors in Munich (1997).

[62] F. Pobell; *Matter and Methods at Low Temperatures.* Springer-Verlag, Berlin, 1992.

[63] G.K. White; *Experimental Techniques in Low-Temperature Physics.* Clarendon Press, Oxford, 1979.

[64] O.W. Lounasmaa; *Experimental Principles and Methods Below 1 K.* Academic Press, London and New York, 1974.

[65] R.C. Richardson and E.N. Smith eds.; *Experimental Techniques in Condensed Matter Physics at Low Temperatures.* Addison-Wesley, Redwood City, CA, 1988.

[66] J.R. Primack, D. Seckel and B. Sadoulet; *Detection of Cosmic Dark Matter.* Ann. Rev. Nucl. Part. Sci. **38** (1988) 751-807.

[67] A. Alessandrello et al.; *A new search for neutrinoless $\beta\beta$ decay with a thermal detector.* Phys. Lett. **B335** (1994) 519.

[68] P. Schmüser; *Superconductivity.* Proceedings of the CERN accelerator school, superconductivity in particle accelerators, hold in Hamburg in May 1995, ed. S. Turner; CERN 96-03, Geneva 1996.

[69] H.K. Onnes, Comm. Leiden **120 b** (1911)

[70] H.K. Onnes, Comm. Leiden, Suppl. Nr. 34 (1913)

[71] W. Meissner and R. Ochsenfeld, Naturwissenschaften **21** (1933) 787.

[72] E. Maxwell; *Isotope Effect in the Superconductivity of Mercury.* Phys. Rev. **78** (1950) 477.

[73] C.A. Reynolds, B. Serin, W.H. Wright and L.B. Nesbitt; *Superconductivity of isotopes of Mercury.* Phys. Rev. **78** (1950) 487.

[74] N.W. Ashcroft and N.D. Mermin; *Solid State Physics.* HRW International Edition, Saunders College, Philadelphia, 1976.

[75] W. Buckel; *Supraleitung – Grundlagen und Anwendungen*, 5. Edition, VCH Verlagsgesellschaft mbH, Weinheim, 1994.

[76] J. Bardeen, L.N. Cooper and J.R. Schrieffer; *Theory of Superconductivity.* Phys. Rev. **108** (1957) 1175-1204.

[77] D. Twerenbold; *Gryogenic Particle Detectors.* Rep. Prog. Phys. **59** (1996) 349.

[78] N.E. Booth, B. Cabrera and E. Fiorini; *Low-Temperature Particle Detectors.* Annu. Rev. Nucl. Sci. **46** (1996) 471-532.

[79] Proceedings of the Workshop *Low Temperature Detectors for Neutrinos and Dark Matter*; eds. K. Pretzl, N. Schmitz and L. Stodolsky, Sprioger-Verlag, Berlin, 1987.

[80] Proceedings of the second Workshop on *Low Temperature Detectors for Neutrinos and Dark Matter*; eds. L. Gonzales-Mestres and D. Perret-Gallix, Editions Frontières, Gif-sur-Yvette, France, 1988.

[81] Proceedings of the third Workshop on *Low Temperature Detectors for Neutrinos and Dark Matter*; eds. L. Brogiato, D.V. Camin and E. Fiorini, Editions Frontières, Gif-sur-Yvette, France, 1990.

[82] Proceedings of the fourth Workshop on *Low Temperature Detectors for Neutrinos and Dark Matter*; eds. N.E. Booth and G.L. Salmon, Editions Frontières, Gif-sur-Yvette, France, 1992.

[83] Proceedings of the fifth Workshop on *Low Temperature Detectors*; eds. S.E. Labov and B.A. Young, Journal of Low Temperature Physics **93** (1993).

[84] Proceedings of the sixth Workshop on *Low Temperature Detectors*; eds. H.R. Ott and A. Zehnder, Nucl. Instr. and Meth. **A370** (1996).

[85] Proceedings of the seventh Workshop on *Low Temperature Detectors*; ed. S. Cooper, Munich, 1997.

[86] K.D. Irwing; *An application of electrothermal feedback for high resolution cryogenic particle detection* Appl. Phys. Lett. **66** (1995) 1998.

[87] D. Twerenbold; *Developing transition edge sensors for mass spectrometry of biological macromolecules.* Not published. June 1995.

[88] D. Twerenbold; *Superconducting Tunneling Junctions as X-Ray Detectors and their Possible Applications in Astrophysics.* Nucl. Instr. and Meth. **A273** (1988) 575.

[89] D. Twerenbold; *Giaever-Type Superconducting Tunneling Junctions as High-Resolution X-Ray Detectors.* Thesis, Diss. ETH No. 8038, Zurich, 1986.

[90] D. Twerenbold; *Nonequilibrium model of the superconducting tunneling X-ray detector.* Phys. Rev. B **34** (1986) 7748-7759.

[91] D. Twerenbold; *The Maximol Area of Superconducting Tunneling Junction X-Ray Detectors Determined by the Required Signal-To-Noise Ratio.* Nucl. Instr. Metb. **A260** (1987) 430-436.

[92] M. Nahum, J.M. Martinis and S. Castles; *Hot-electron microcalorimeters for X-ray and phonon detection.* Pages 733-738 in [83].

[93] M. Nahum and J.H. Martinis; *Hot-electron microcalorimeters as high-resolution X-ray detectors.* Appl. Phys. Lett. **66** (1995) 3203-3205.

[94] J.H. Martinis; *Hot-electron-microcalorimaters with 0.25 mm^2 area.* Pages 171-172 in [84].

[95] K.D. Irwing, G.C. Hilton, J.M. Martinis and B. Cabrera; *A hot-electron microcalorimeter for X-ray detection using a superconducting transition edge sensor with electrothermal feedback.* Pages 177-179 in [84].

[96] M. Nahum, T.M. Eiles and J. Martinis; *Electronic microrefrigerator based on a normal-insulator-superconductor tunnel junction.* Appl. Phys. Lett. **65** (1994) 3123-3125.

[97] B. van den Brandt, J.A. Konter and S. Mango; *A compact versatile dilution refrigerator with top-loading capability*, Nucl. Instr. and Meth. **A289** (1990) 526-531.

[98] D. Twerenbold; *Giaver-type superconducting tunneling junctions as high-resolution X-ray detectors.* Europhys. Lett. **1** (1986) 209-214.

[99] H. Kraus, Th. Peterreins, F. Prőbst, F. v. Feilitzsch, R.L. Mősshauer, V. Zacek and E. Umlauf; *High-resolution X-ray detection with superconducting tunnel junctions.* Europhys Lett. **1** (1986) 161.

[100] R.P. Welty and J.M. Martinis; *A series array of DC SQUIDS.* IEEE Trans. Appl. Supercond. **3** (1993) 2605.

[101] A.F. Andreev; *The thermal conductivity of the intermediate state in superconductors.* Sov.Phys. JETP **19** (1964) 1228.

[102] J.-L. Berchier and D.H. Sanchez; *Fabrication techniques for microdevices in soft superconductors.* Rev. Sci. Instrum. **49** (1978) 1452-1459.

[103] Y. de Coulon; *Jonctions supracondutrices a effet tunnel comme detecteurs de particules,* Ph.D. thesis, University of Neuchâtel, 1989.

[104] C. Grosjean; *Fabrication de jonctions supraconductrices a effet tunnel comme détecteurs cryogéniques de particules dans un spectromètre à temps-de-vol MALDI,* diploma work, University of Neuchâtel, 1997.

[105] S. Schuerch, M. Schaer, K.O. Boernsen and U.P. Schlunegger; *Enhanced Mass Resolution in Matrix-assisted Laser Desorption/Ionization Linear Time-of-flight Mass Spectrometry.* Biol. Mass Spectrom **23** (1994) 695-700.

[106] K.J. Wu, A. Steding and C.H. Becker; Rapid. Commun. Mass Spectrom. **7** (1993) 142.

Acknowledgments

Firstly, I would like to express thanks to Professor Jean-Luc Vuilleumier for providing the possibility for me to be engaged in this project and for his support throughout this work.

Special thanks is given Dr. Damian Twerenbold for his enthousiasmic guidance and experimental competence.

I wish to thank Professor Piero Martinoli for supporting this project and for allowing us to use his cleanroom facility. I should also thank the members of his group, especially Dr. Peter Scheuzger and Bertrand Schmied for introducing me into the field of photolithography and Dr. Chris Leemann for enlightening discussions.

My gratitude goes to Dr. Almut Tadsen for introducing me to cryogenics and to both my diploma students Angèle Tripet and Chantal Grosjean for their valuable contribution.

I thank Professor Ernst Schumacher for having taken time to be member of my thesis jury and for enlightening advice.

Thanks go also to all members of the technical staff for having offered me – not allways but quite often – small wonders in a reasonable time lap, and I am thankful to anyone else who helped me to accomplish my work.

Finally I would like to thank my parents for their support and Gordana for all her love.

Neuchâtel, October 1997.